



## A detailed analysis of the February 1996 aftershock sequence in the eastern Pyrenees, France

Hélène Pauchet, Alexis Rigo, Luis Rivera, Annie Souriau

### ► To cite this version:

Hélène Pauchet, Alexis Rigo, Luis Rivera, Annie Souriau. A detailed analysis of the February 1996 aftershock sequence in the eastern Pyrenees, France. *Geophysical Journal International*, 1999, 137 (1), pp.107-127. 10.1046/j.1365-246x.1999.00776.x . hal-03198583

HAL Id: hal-03198583

<https://hal.science/hal-03198583>

Submitted on 18 Jun 2021

**HAL** is a multi-disciplinary open access archive for the deposit and dissemination of scientific research documents, whether they are published or not. The documents may come from teaching and research institutions in France or abroad, or from public or private research centers.

L'archive ouverte pluridisciplinaire **HAL**, est destinée au dépôt et à la diffusion de documents scientifiques de niveau recherche, publiés ou non, émanant des établissements d'enseignement et de recherche français ou étrangers, des laboratoires publics ou privés.

# A detailed analysis of the February 1996 aftershock sequence in the eastern Pyrenees, France

Hélène Pauchet,<sup>1</sup> Alexis Rigo,<sup>1</sup> Luis Rivera<sup>2</sup> and Annie Souriau<sup>1</sup>

<sup>1</sup>Observatoire Midi-Pyrénées, GRGS-CNRS UMR 5562, 14 Ave. E. Belin, 31400 Toulouse, France. E-mail: Alexis.Rigo@cnes.fr

<sup>2</sup>EOPG, 5 rue René Descartes, 67084 Strasbourg, France

Accepted 1998 October 18. Received 1998 September 4; in original form 1997 December 31

## SUMMARY

Following the 1996 February 18  $M_L = 5.2$  earthquake in the Agly massif in the eastern French Pyrenees, we installed a temporary network of seismometers around the epicentre. In this paper, we analyse 336 well-located aftershocks recorded from February 19 to February 23 by 18 temporary stations and two permanent stations located less than 35 km from the epicentre. Most aftershocks have been located with an accuracy better than 1.5 km in both horizontal and vertical positions. Their spatial distribution suggests the reactivation of a known fault system. We determined 39 fault-plane solutions using  $P$ -wave first motions. Despite their diversity, the focal mechanisms yield an E–W subhorizontal T-axis. We also determined fault-plane solutions and principal stress axes using the method developed by Rivera & Cisternas (1990) for the 15 best-recorded events. We obtain a pure-shear-rupture tectonic regime under N–S subhorizontal compression and E–W subhorizontal extension. These principal stress axes, which explain the focal mechanisms for at least 75 per cent of the 39 aftershocks, are different from the axes deduced from the main shock. The post-earthquake stress field caused by the main-shock rupture, modelled as sinistral strike slip on three vertical fault segments, is computed for various orientations and magnitudes of the regional stress field, assumed to be horizontal. The aftershock distribution is best explained for a compressive stress field oriented N30°E. Most aftershocks concentrate where the Coulomb failure stress change increases by more than 0.2 MPa. The diversity of aftershock focal mechanisms, poorly explained by this model, may reflect the great diversity in the orientations of pre-existing fractures in the Agly massif.

**Key words:** aftershocks, fault-plane solutions, Pyrenees, seismotectonics, stress distribution.

## 1 INTRODUCTION

On 1996 February 18, an  $M_L = 5.2$  earthquake occurred in the eastern Pyrenees, France (Fig. 1). This event is the largest in the range since the Arette earthquake ( $M = 5.7$ ) in 1967 (Gagnepain-Beyneix *et al.* 1982). Fortunately, no one was hurt and the damage in nearby villages was minor. The main shock and the major aftershocks over a period of 2 months have been studied by Rigo *et al.* (1997). Following the main shock, a temporary network of seismometers was installed and recorded hundreds of aftershocks between 1996 February 19 and 23.

The Pyrenean range is the result of the continental collision between the Iberian and Eurasian plates. The north–south convergence of the two plates began during the upper Cretaceous (65 Ma) after an extensional episode related to the opening of the Bay of Biscay during the lower Cretaceous

(80–120 Ma). Vertical reflection profiles (ECORS Pyrenees team 1988; Choukroune & ECORS team 1989; Choukroune *et al.* 1990; Mattauer 1990; Choukroune 1992; Suriñach *et al.* 1993) and tomographic models (Souriau & Granet 1995) favour a continental subduction of the Iberian lower crust beneath the Eurasian lower crust, at least in the central and eastern parts of the range. Finally, the eastern end of the range has been affected by a phase of NW–SE extension which began in late Eocene time. This last phase corresponds to the opening of the Gulf of Lion and the eastward migration of the Corso–Sardinian block (Rehaut *et al.* 1984).

The North Pyrenean Fault is considered to be the boundary between the Iberian and Eurasian plates. This fault, which runs E–W throughout the range, offsets the Moho vertically, with thicker crust on the Iberian side. The Moho offset reaches 15 km in the central part of the range (Hirn *et al.* 1980; Gallart *et al.* 1981; Daignières *et al.* 1982; Choukroune & ECORS

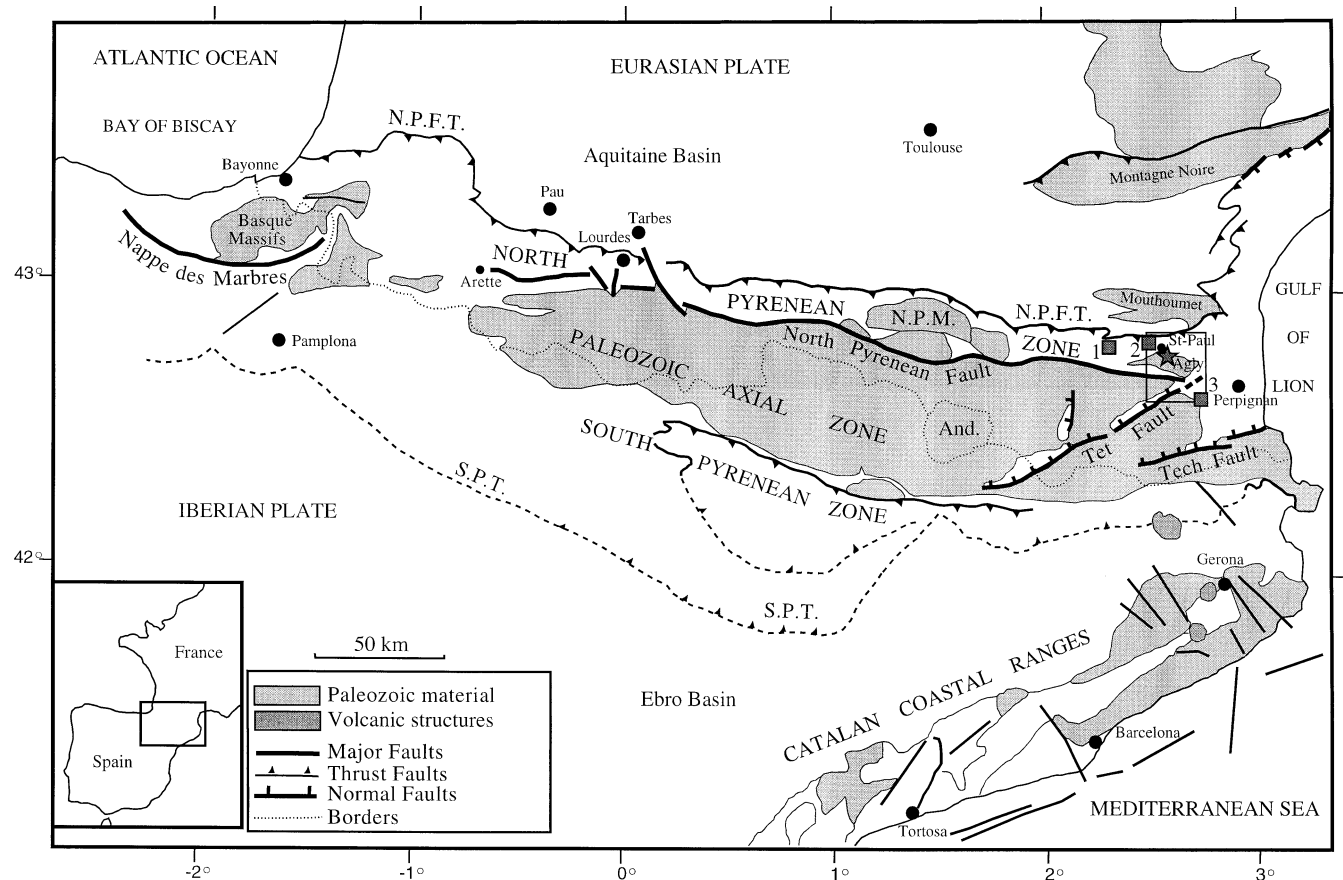


**Figure 1.** Main structural units of the Pyrenees. The box including the Agly massif and the town of Saint-Paul de Fenouillet is the region of interest shown in Figure 2. The star is the 1996 February 18 main-shock epicentre. Squares show historical earthquakes in the eastern Pyrenees [1: 1920 November 28 earthquake with MSK intensity  $I = V\text{--}VI$ ; 2: 1922 September 23 earthquake,  $I = VI\text{--}VII$ ; 3: 1922 December 28 earthquake,  $I = VI$  (Cadiot *et al.* 1979; Lambert & Levret-Albaret 1996)]. N.P.F.T.: North Pyrenean Frontal Thrust; N.P.M.: North Pyrenean Massifs; S.P.T.: South Pyrenean Thrust; And: Andorra.

team 1989), but it does not exceed 5 km in the eastern part (Gallart *et al.* 1980, 1982). At the eastern end of the Pyrenean range, in the Gulf of Lion and along the Iberian Mediterranean margin, major normal faults are present with NE–SW to E–W strikes (Briais *et al.* 1990).

The 1996 earthquake occurred near the town of Saint-Paul de Fenouillet in the Agly massif, 8 km north of the North Pyrenean Fault (Fig. 1). The Agly massif is a Palaeozoic outcrop included in the North Pyrenean Zone, which is composed mainly of highly deformed Mesozoic flysch deposits (Puigdefabregas & Souquet 1986). The Agly massif consists of Hercynian granitic and metamorphic rocks. Uplift of these granulitic facies rocks took place during the extensional episode, ending during the upper Cretaceous (Delay 1989). During the Alpine phase of the Pyrenean orogeny, the Agly massif fractured, developing strike-slip faults mostly oriented N110°E. These faults were then distorted during the Oligocene, leading to local perturbations in strike (Fonteilles 1970; Delay 1989) (Fig. 2).

Instrumental seismicity recorded during the last 33 years (Gagnepain-Beyneix *et al.* 1997; Souriau & Pauchet 1998) shows fewer than 30 events in the Saint-Paul de Fenouillet region (Fig. 2). The six strongest events had magnitudes between 3.0 and 3.5. Three historical earthquakes occurred in

this area, one in 1920 and two in 1922 (Fig. 1), with MSK intensities of about V–VI, VI–VII and VI, respectively (Cadiot *et al.* 1979; Lambert & Levret-Albaret 1996).

Rigo *et al.* (1997) located the main shock at 42°47.81'N and 2°32.30'E, with a depth of about 7.7 km. The uncertainties are about  $\pm 1.5$  km for the epicentral position and  $\pm 2.5$  km for the focal depth. No surface rupture was observed. The focal mechanism has an E–W-striking subvertical nodal plane and a N–S-striking nodal plane dipping 47°W (Fig. 2). This mechanism is very well constrained; the uncertainties on the strike and dip for both nodal planes are about  $\pm 5^\circ$ . The E–W nodal plane must be the active plane considering the E–W trends of the major faults in the Agly massif. Thus, the mechanism of the rupture is E–W left-lateral strike-slip faulting with a small normal-faulting component. This mechanism is consistent with the E–W sinistral motion previously observed for a 1981 earthquake ( $M_L = 4.5$ ) located on the North Pyrenean Fault, 50 km west of Saint-Paul de Fenouillet (Gallart *et al.* 1982; Olivera *et al.* 1986). These results suggest tectonic heterogeneity in the Pyrenean range, with a sinistral tectonic regime in this eastern part, whilst a dextral tectonic regime is inferred in the western part of the range from the focal solutions of the 1967 Arette event ( $M = 5.7$ ) and from the analysis of small earthquakes (Gagnepain *et al.* 1980). Controversy over the

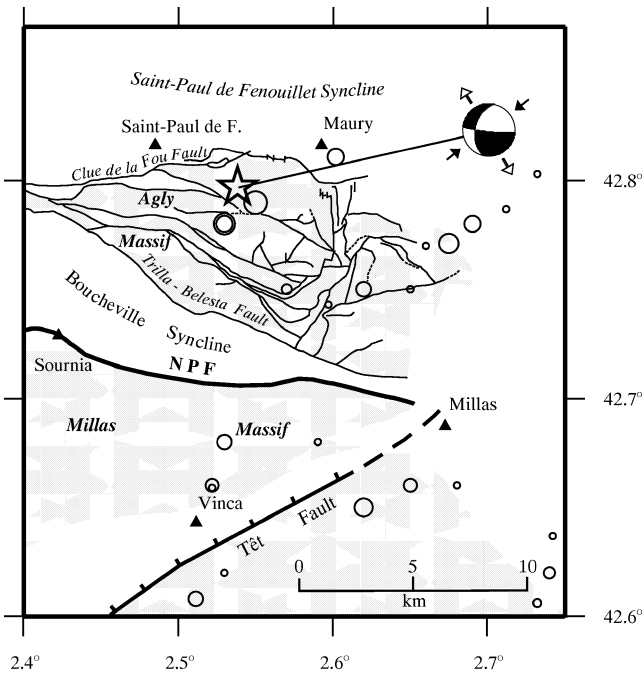


**Figure 2.** Tectonic map of the Agly massif (redrawn from Delay 1989) and instrumental seismicity recorded by the regional permanent seismic network from its installation (January 1989) to the main-shock occurrence (February 1996). The symbol size is proportional to the magnitude  $M_I$  (from 1.0 to 3.4). The star represents the main-shock epicentre. The main-shock fault-plane solution is also indicated (lower equal-area hemisphere), with its compressional (P-) and extensional (T-) axes (black and white arrows, respectively) from Rigo *et al.* (1997). The shaded areas correspond to the Palaeozoic massifs and the white areas to the Mesozoic basins. NPF: North Pyrenean Fault.

contemporary tectonic regime in the eastern part of the range has arisen from the interpretation of the large seismic crisis of 1427–1428 in Catalonia. Some authors favour a general NW–SE extension through to the present (Briais *et al.* 1990), whilst others argue for a N–S compressive regime (Philip *et al.* 1992). The normal component of the main-shock fault-plane solution favours the former. In the following, we will carry out a careful analysis of the aftershocks of the February 1996 Agly event in order to map the rupture plane in three dimensions and to try to constrain the stress regime in that part of the range.

## 2 LOCAL NETWORK AND DATA ACQUISITION

The main shock and the first major aftershocks were recorded by the permanent seismological network of the Pyrenees, with 10 stations less than 65 km from the epicentre. Then, 19 hr after the main shock, a first portable station (SPF) was installed at the main-shock epicentre (Fig. 3). This station allowed us to follow the aftershock sequence in time and depth (Rigo *et al.* 1997). Short-period instruments were then deployed to complete the temporary network 30 hr after the main shock. This network included 19 three-component stations and nine one-component stations from the French ‘Institut National des Sciences de l’Univers’ (Table 1). We also used the data from two three-component stations (ANSZ and MILZ) installed at the same time by the ICC/SGC (Institut Cartographique de Catalogne/Servei Geològic de Catalunya, Barcelona).

Unfortunately, inclement weather (10 cm of snow in the first 12 hr) caused some instruments to malfunction, particularly

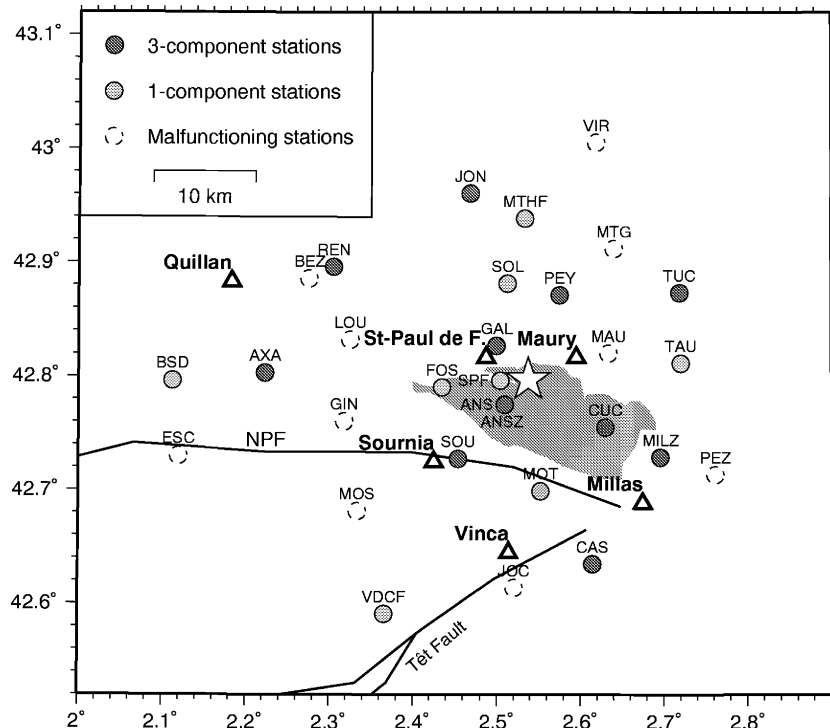


**Figure 3.** Temporary seismological stations installed between 18 and 23 February 1996, in a radius of 35 km around the 1996 February 18 main-shock epicentre (star). MTHF and VDCF are two stations of the permanent network. The shaded area corresponds to the Agly massif. Dashed circles are stations which did not work during the duration of the experiment. NPF: North Pyrenean Fault.

**Table 1.** Coordinates and characteristics of the temporary seismographic stations installed between 18 and 23 February 1996.

Stations code	Latitude	Longitude	Height m	No. channels	Record type	Sample rate
ANS	42°46.49'	2°30.58'	275	3	trigger digital	76
ANSZ	42°46.50'	2°30.39'	275	3	continuous digital	100
AXA	42°48.16'	2°13.37'	550	3	continuous digital	100
BEZ	42°53.14'	2°16.54'	530	3	trigger digital	76
BSD	42°47.78'	2°06.74'	1100	1	continuous digital	62.5
CAS	42°38.09'	2°36.89'	430	3	continuous digital	100
CUC	42°45.29'	2°37.82'	270	3	continuous digital	100
ESC	42°43.78'	2°07.18'	1140	3	trigger digital	76
FOS	42°47.42'	2°26.10'	570	1	continuous analogue	
GAL	42°49.61'	2°29.99'	363	3	continuous digital	100
GIN	42°45.62'	2°19.07'	804	3	trigger digital	76
JOC	42°36.84'	2°31.24'	383	3	trigger digital	76
JON	42°57.66'	2°28.13'	672	3	continuous digital	100
LOU	42°49.93'	2°19.50'	858	1	trigger digital	76
MAU	42°49.20'	2°38.04'	193	3	trigger digital	76
MILZ	42°43.71'	2°41.75'		3	continuous digital	100
MOS	42°40.87'	2°20.00'	969	3	trigger digital	76
MOT	42°41.93'	2°33.14'	419	1	continuous analogue	
MTG	42°54.72'	2°38.42'	385	3	trigger digital	76
MTHF	42°56.32'	2°32.04'	550	1	trigger digital	50
PEY	42°52.27'	2°34.54'	268	3	continuous digital	100
PEZ	42°42.79'	2°45.68'	115	3	trigger digital	76
REN	42°53.78'	2°18.30'	415	3	continuous digital	100
SOL	42°52.88'	2°30.79'	504	1	continuous analogue	
SOU	42°43.63'	2°27.25'	155	3	continuous digital	100
SPF	42°47.76'	2°30.27'	364	1	continuous analogue	
TAU	42°48.68'	2°43.21'	374	1	continuous analogue	
TUC	42°52.41'	2°43.13'	375	3	continuous digital	100
VDCF	42°35.45'	2°21.92'	605	1	trigger digital	50
VIR	43°00.32'	2°37.13'	345	3	trigger digital	76

for timing. In the end, 20 stations provided good-quality data. Despite these difficulties, we obtained a good spatial distribution of the stations with an average distance between stations of 5 km (Fig. 3).

From February 19–23, more than 1200 events were recorded. The accuracy of the *P*-arrival time readings depends upon the type of record, the sample rate and the noise level (Table 1). We estimated the *P*-wave time-reading error to be 0.03 s for

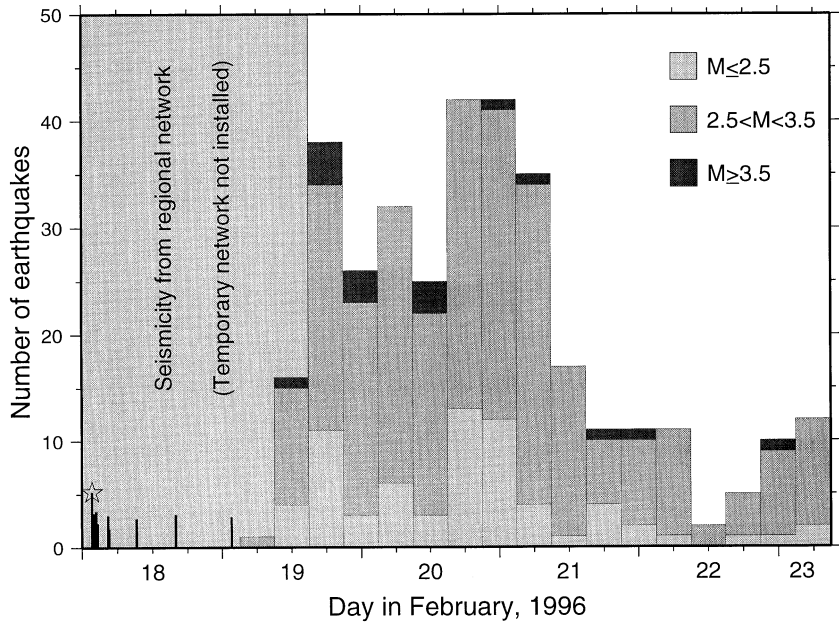


**Figure 4.** Number of earthquakes per 6 hr versus time during the five days after the main shock (star), with an indication of magnitudes (grey scale). During the first 30 hr, lines denote events recorded by the permanent network; their lengths are proportional to magnitude  $M_I$  (from 1.8 to 5.2).

the digital records and 0.1 s for the analogue records. For the S waves, the accuracy is poorer, no better than 0.05 s in the best cases.

### 3 EVENT LOCATIONS

Hypocentral locations were computed with the HYPO71 code (Lee & Lahr 1975) using the *P*-and *S*-wave arrival times. We used a multilayered *P*-velocity model (Table 2) deduced from seismic refraction profiles (Gallart *et al.* 1981; Daignières *et al.* 1982). A  $V_p/V_s$  ratio of 1.75 is used; this was previously

**Table 2.** *P*-velocity models used for the earthquake locations. The  $V_p/V_s$  ratio used is 1.75.

Depth (km)	<i>P</i> -velocity model ( $\text{km s}^{-1}$ )	
	Multilayered	Two-layered
0.0–1.0	5.5	
1.0–4.0	5.6	6.2
4.0–10.0	6.1	
11.0–34.0	6.4	
> 34.0	8.0	8.0

determined using the Wadati method from 15 years of regional seismicity (Njike Kassala *et al.* 1992). Among the 1200 recorded events, we retained only those which met the following four conditions: (1) traveltimes residuals of less than 0.4 s; (2) a hypocentral location uncertainty of less than 3 km; (3) at least six legible arrival times; (4) an azimuthal gap of less than  $180^\circ$ . We obtain a final set of 336 events (Appendix A). The mean rms traveltimes residual for these events is  $0.13 \pm 0.08$  s. The mean horizontal error given by the computation is 0.87 km and the mean vertical error is 0.99 km. To appraise the actual accuracy of hypocentre determinations, we investigated the influence of the crustal velocity model. The solutions are mainly sensitive to the *P*-velocity model used for the inversion. Using a homogeneous crust instead of a multilayered crust (Table 2) results in shifts of less than 1.5 km for almost all epicentral positions and less than 1 km for almost all depths. We thus conclude that uncertainties are about 1.5 km for the hypocentre determinations.

For the retained events, the magnitudes range between 2.1 and 4.0. Magnitudes have been determined from coda-wave duration and are not calibrated to the regional network. The difference between our magnitudes and those obtained from the regional network may reach 1.0 for the smallest events.

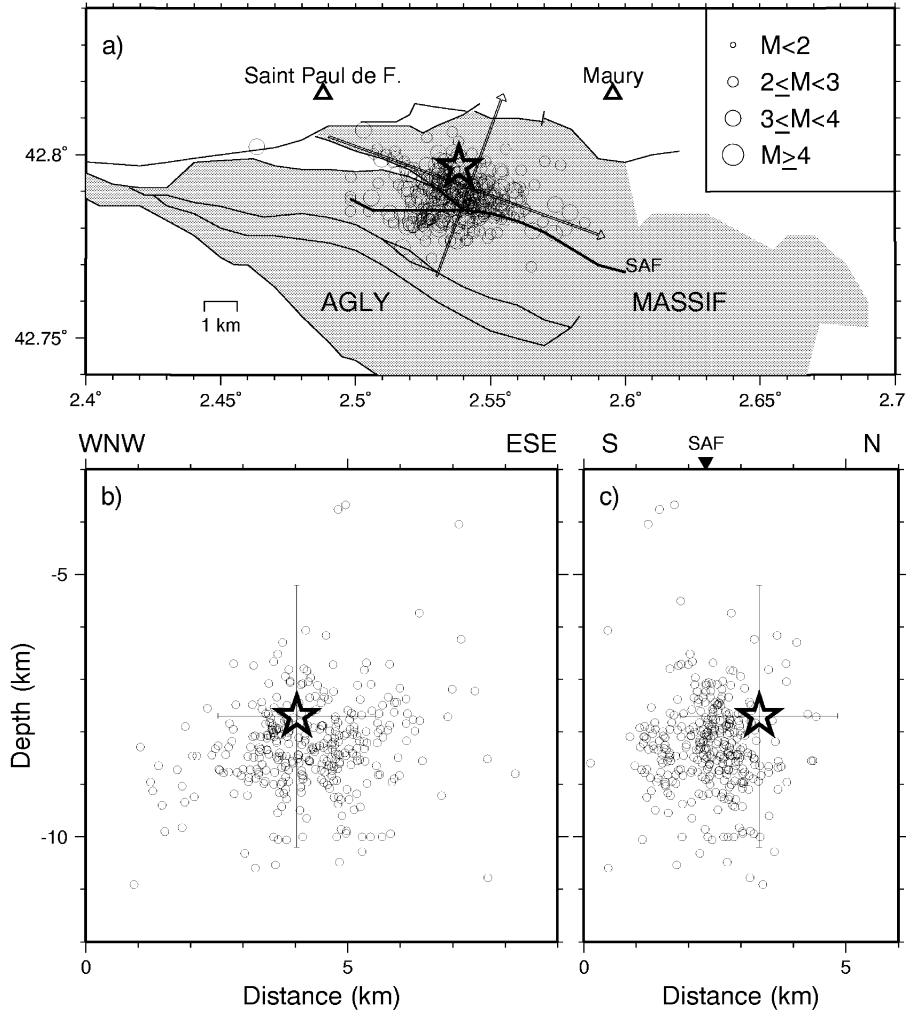


**Figure 5.** (a) Epicentral locations of the aftershocks with symbol size indicating magnitude. Arrows indicate the lengths and directions of the cross-sections. (b) N110°E cross-section. (c) N20°E cross-section. All the aftershocks are projected on each cross-section. Error bars are for the main shock (star). Shaded area corresponds to the Agly massif. SAF: Saint-Arnac Fault.

One and a half days after the main shock, the recorded seismic activity consisted of about 10 events per hour in our final data set. Before this time, only a few large events were recorded by the permanent network. After February 21, only one event with magnitude larger than 3.5 occurred (Fig. 4). The entire aftershock sequence lasted at least 77 days (Correig *et al.* 1997).

The aftershocks form a cluster covering an area of approximately  $4.5 \times 7$  km trending WNW–ESE (Fig. 5a). This orientation is compatible with the main orientation ( $N110^\circ E$ ) of the major faults mapped in the Agly massif, and justifies the choice of the E–W nodal plane as the rupture plane for the main shock. In the western part, the cluster seems to split into two branches, which coincide with two segments of the Saint-Arnac Fault (Fig. 5a). This leads to the postulation that both the southern and the northern E–W-striking fault segments ruptured in this sequence.

Figs 5(b) and (c) show cross-sections in the directions  $N110^\circ E$  and  $N20^\circ E$ , respectively. Aftershocks are located

between 5 and 11 km in depth. The main shock (Rigo *et al.* 1997) falls inside this cluster, if we take into account the error bars on its location. The aftershock distribution delimits a  $5 \times 7$  km zone, which is compatible with the magnitude of the main shock (Hanks & Kanamori 1979). The aftershock pattern is complex: the N–S extent of the seismicity strip is rather large (3–4 km), as shown in Fig. 5(c). This indicates, as already observed on map, that the rupture did not involve a single plane. To the south, the seismicity involves the southern fault segment of the Saint-Arnac Fault.

#### 4 FAULT-PLANE SOLUTIONS

We determined focal mechanisms for 39 aftershocks using the polarities of the  $P$ -wave first motions. The magnitudes for these events range from 2.7 to 3.9. Thanks to the good azimuthal coverage provided by our stations, we were in some cases able to determine well-constrained focal mechanisms

**Table 3.** Focal mechanism parameters. (a): focal mechanisms determined from P-first motions. (b): focal mechanisms issued of the stress tensor inversion.

Date yymmdd	Time hh:mm	Strike 1 (°) (a)	Dip 1 (°) (a)	Rake 1 (°) (a)	Strike 2 (°) (a)	Dip 2 (°) (a)	Rake 2 (°) (a)
		(b)	(b)	(b)	(b)	(b)	(b)
960219	14:44	259.0	66.0	38.6	151.0	55.2	150.3
960219	16:04	103.0	115.2	53.0	210.0	68.8	40.2
960219	17:49	257.0	62.0	−105.8	108.0	31.8	−63.0
960219	20:25	66.0	59.3	66.0	333.0	327.3	149.8
960219	21:14	80.0	33.5	26.0	34.0	260.0	155.8
960219	22:14	320.0	314.1	77.0	273.5	64.0	116.6
960219	22:27	198.0	89.0	−63.4	77.0	198.1	98.8
960220	00:06	323.0	329.6	23.0	290.0	13.2	153.2
960220	05:03	48.0	61.0	22.2	−112.3	149.0	29.4
960220	06:31	279.0	278.5	34.0	−112.9	68.8	−80.9
960220	08:55	359.0	326.0	29.0	174.1	69.6	−81.0
960220	09:22	279.0	264.8	51.0	−134.5	−80.9	−94.3
960220	11:21	276.0	267.2	49.7	170.0	−70.9	−70.1
960220	12:34	306.0	276.0	30.0	101.8	−143.0	102.8
960220	12:58	354.0	354.7	30.6	−162.8	41.6	59.5
960220	14:27	252.0	354.0	44.0	176.0	97.0	107.1
960220	15:27	185.0	194.0	56.0	171.0	−142.6	122.2
960220	16:27	344.0	185.0	86.0	0.0	90.0	−142.4
960220	16:32	30.0	344.0	46.0	17.7	103.5	178.3
960220	17:20	40.0	30.0	154.9	95.0	90.0	46.8
960220	19:35	83.0	40.0	69.0	92.0	56.0	−154.4
960220	21:38	316.0	83.0	74.0	135.0	54.1	−160.1
960220	22:19	273.0	316.0	48.0	−37.6	175.0	−158.9
960220	23:39	140.0	273.0	50.0	−74.8	84.8	−143.5
960220	23:39	140.0	140.0	50.0	−164.7	44.0	−105.4
960220	23:39	15.0	140.0	50.0	−164.7	40.0	−41.0
960221	01:15	28.0	15.0	47.0	−56.6	40.0	−41.0
960221	01:44	338.0	28.0	51.0	151.0	52.4	−120.5
960221	01:45	317.0	338.0	52.0	−91.3	59.0	−88.4
960221	02:06	352.0	317.0	54.9	−88.2	39.0	−92.4
960221	02:47	306.0	352.0	−99.6	155.0	39.0	−136.0
960221	03:31	50.0	306.0	43.0	−43.4	−81.2	161.6
960221	03:38	68.0	50.0	54.9	150.0	−92.3	92.1
960221	04:35	304.0	68.0	61.0	−86.7	−149.5	−149.5
960221	05:11	249.0	304.0	70.0	87.8	335.0	159.8
960221	06:50	3.0	249.0	47.0	−20.0	64.0	50.7
960222	02:53	14.0	3.0	52.0	139.8	61.8	75.1
960222	07:07	360.0	14.0	61.0	161.0	39.6	−108.1
960223	00:06	300.0	360.0	10.0	73.2	−71.3	−107.3
					−30.2	127.0	−162.9
					10.2	129.2	79.8
					−11.5	77.9	−108.1
					279.0	79.0	−93.2
					106.4	80.5	113.1
					153.0	49.0	−162.9

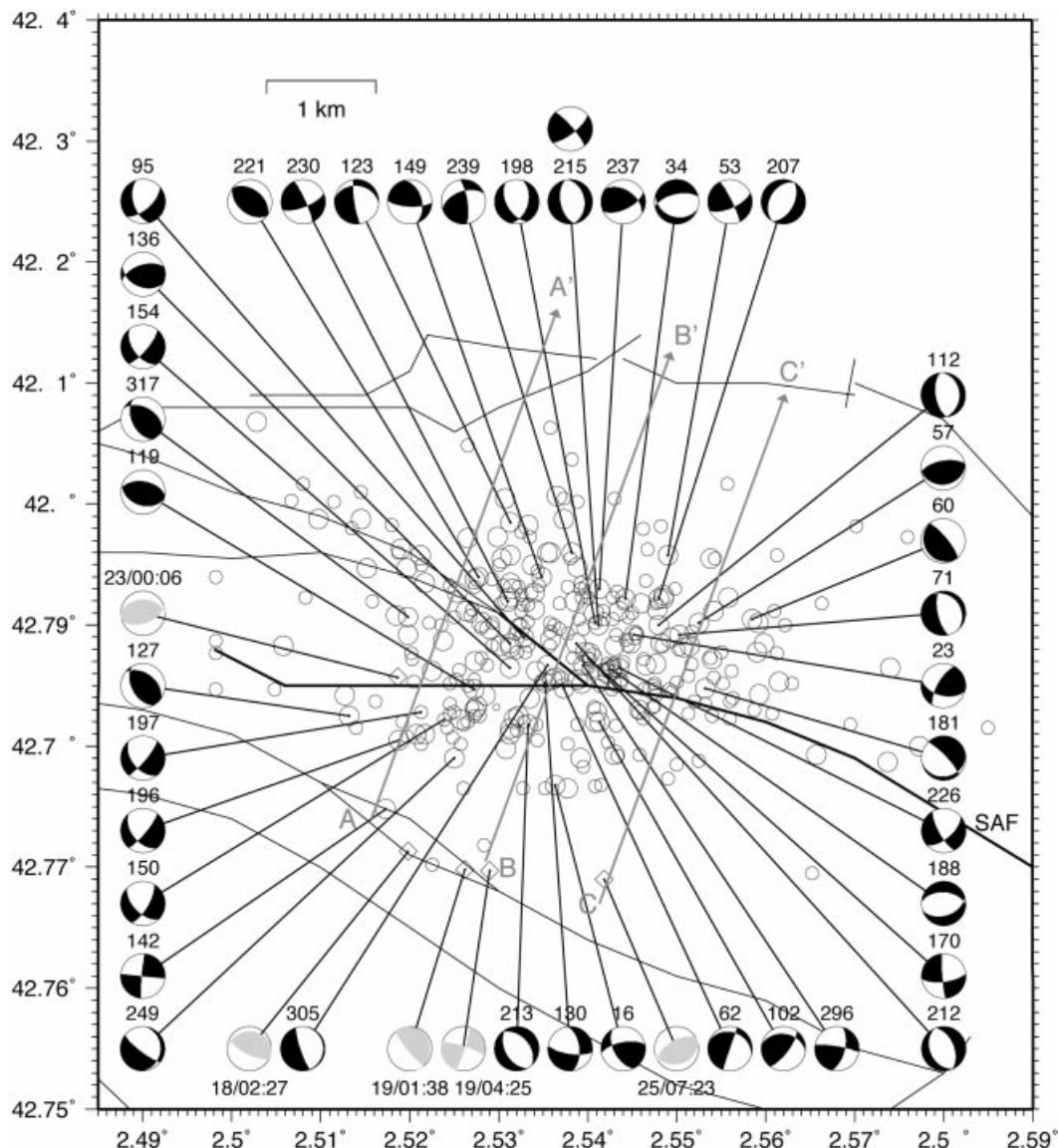
with only six clear  $P$  polarities (for example the February 20 event at 12:34, see Appendix B). We estimated the uncertainties of the strikes and dips of the nodal planes to be about  $\pm 15^\circ$  (Table 3).

Fig. 6 shows a rather large diversity of focal mechanisms: normal-faulting mechanisms (21) for the major part of our set, reverse-faulting mechanisms (13) and some strike-slip-faulting mechanisms (5). Reverse, normal and strike-slip mechanisms occur close to each other and it is difficult to identify sequences of events with similar features. We also report the five fault-plane solutions determined by Rigo *et al.* (1997) for events before and after our time window. Most of these events seem to be located on a NW–SE-striking fault south of the Saint-Arnac Fault, but no significant activity has been recorded by the temporary network along this fault. We have checked that there is a systematic shift between the locations determined from the permanent network and those determined from the temporary network; these events are very probably located

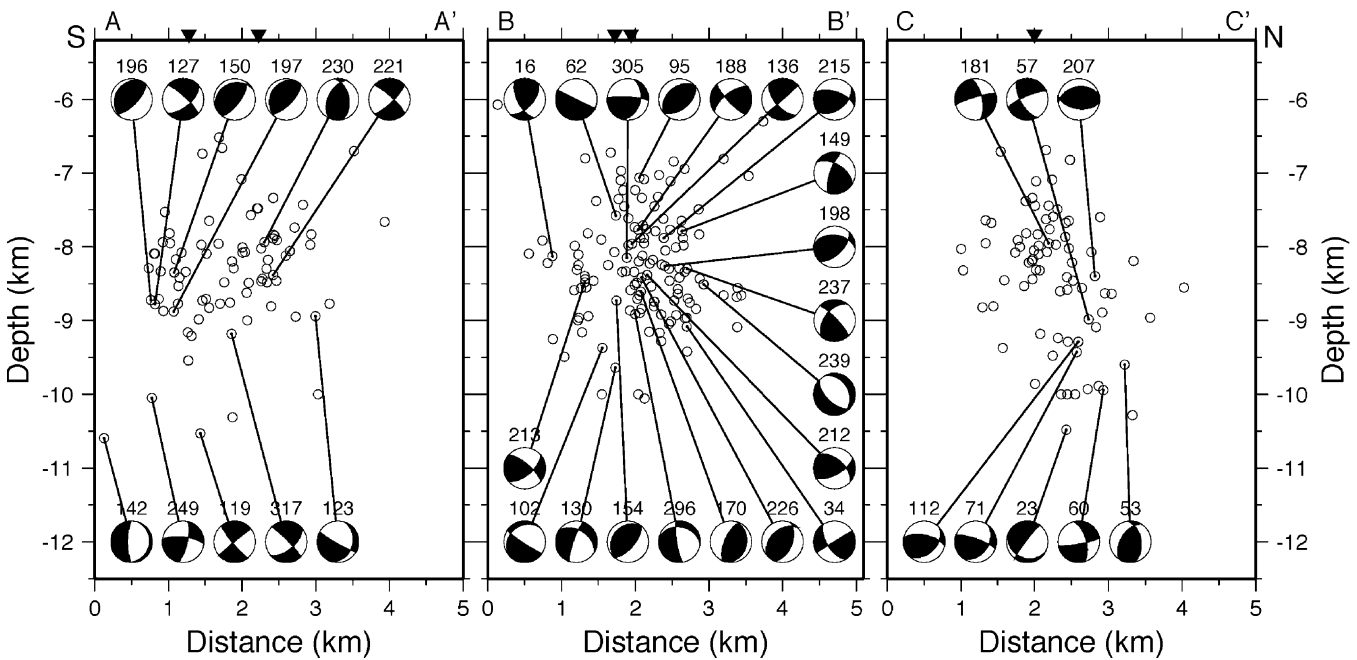
inside the main cluster north of the kink of the Saint-Arnac Fault.

Fig. 7 shows a projection of all aftershock locations and fault-plane solutions on three N20°E cross-sections mapped in Fig. 6. Like the map distribution, the pattern of fault-plane solutions is rather complex.

We have represented the  $P$ ,  $T$  and  $N$  axes deduced from the fault-plane solutions on normalized rose diagrams (Fig. 8). The extensional  $T$ -axes exhibit a clear E–W orientation with a subhorizontal plunge. The  $P$  and  $N$  axes are more scattered. This scatter may be the expression of slip on pre-existing fractures with various orientations. The subhorizontal  $P$ -axes correspond to reverse and strike-slip faults, whereas the subhorizontal  $N$ -axes mostly correspond to normal faults. The axis orientations obtained for the aftershocks are different to those obtained for the main shock, i.e. a SE–NW direction for the extensional  $T$ -axis and a NE–SW direction for the compressional  $P$ -axis (Fig. 2) (Rigo *et al.* 1997).



**Figure 6.** Fault-plane solutions (lower equal-area hemisphere) for 39 selected events (black and white). Numbers at the top of fault-plane solutions refer to Appendix B. The grey and white fault-plane solutions are those determined by Rigo *et al.* (1997). For event 215, a different fault-plane solution was determined by inversion following Rivera & Cisternas (1990). Arrows AA', BB', CC' are the three cross-sections shown in Figure 7.



**Figure 7.** Vertical cross-sections oriented N20°E across the seismic area. All hypocentres and fault-plane solutions are projected onto the vertical plane. The half-width of the projected corridor is 560 m on either side of the cross-section. Top arrows indicate the surface trace of the different segments of the Saint-Arnac Fault.

The coherence observed for the aftershock T-axes suggests that E–W extension may be the predominant stress regime for the aftershock sequence. In order to confirm this result, we have also determined the aftershock principal stress axes using the method developed by Rivera & Cisternas (1990). This method determines the orientation of the principal stress axes and the focal mechanisms from an inversion of the P polarities and take-off angles for all events, assuming that the stress field is nearly homogeneous in the volume associated with the aftershocks. We show in the next section by modelling the local stress field that this assumption is justified. To obtain a well-constrained solution, we choose to apply the method when at least 10 P polarities are available for each event. This limits to 15 the number of available events among the 39 we had previously. Their magnitudes range from 3.3 to 3.9. The focal mechanisms obtained from this stress tensor inversion (Appendix C) are similar to those previously obtained (Appendix B). Indeed, the difference between the two estimates is smaller than the uncertainty for 14 of the 15 events. The exception is the February 21 event at 02:06, for which the inversion gives a strike-slip faulting mechanism, whereas we determined a normal-faulting mechanism (Fig. 6). These new good determinations (95 per cent with correct polarities, the remaining 5 per cent being close to nodal planes) generally confirm the robustness of our fault-plane solutions. The stress components obtained from the inversion correspond to a shape factor  $R$  of 0.4, which defines a shear-rupture tectonic regime. In this context some pure normal and pure reverse pre-existing faulting may coexist (Armijo *et al.* 1982). The principal stresses,  $\sigma_1$  and  $\sigma_3$ , are almost horizontal and oriented N358°E and N260°E, respectively;  $\sigma_2$  is oriented N109°E and dips at 60° (Fig. 9). These principal stress components are fully compatible with at least 75 per cent of the 39 focal mechanisms and with the average orientation of the T-axis previously determined from the rose diagrams.

## 5 DISCUSSION

The  $(\sigma_1, \sigma_2, \sigma_3)$  stresses inferred from the aftershock polarities exhibit orientations which are significantly different to those of the (P, N, T) axes obtained from the main shock (Fig. 9). Major changes in stress orientation following an earthquake have been observed in other cases, for example the 1992 Landers earthquake and its aftershocks (Hauksson 1994). The simplest explanation is that the main shock locally perturbs the regional stress field. However, the apparent 45° anticlockwise rotation of the maximum horizontal stress ( $S_H$ ) inferred from the comparison of P and  $\sigma_1$  may be overestimated, because the P-axis has been determined from a single event on a pre-existing E–W-striking fault. The  $\sigma_1$ ,  $\sigma_2$  and  $\sigma_3$  directions are characteristics of the local state of stress in the aftershock volume during the aftershock sequence and they are different from the regional stress field. On the other hand, the NE–SW direction for the maximum horizontal compression ( $S_H$ ) deduced from the main-shock fault-plane solution is nearly identical to that deduced from two previous  $M_L > 4.0$  earthquakes in 1978 (observations from the Laboratoire de Détection et de Géophysique, Bruyères-le-Châtel, France) and 1981 (Gallart *et al.* 1982) located, respectively, 25 km east and 50 km west of Saint-Paul de Fenouillet. This direction and the global E–W trend of the major structures of the Pyrenean range are in agreement with a sinistral shear tectonic regime in the eastern part of the North Pyrenean Zone and probably of the North Pyrenean Fault.

The stress drop on a fracture is accompanied by an increase of shear stress beyond the end of the fracture and also in the direction perpendicular to the fracture up to a distance of half the rupture length (Das & Scholz 1981). In many cases, the static stress changes may explain the aftershock distribution (Stein & Lisowski 1983; King *et al.* 1994). In our case, the main event occurred near the junction of three fault segments.

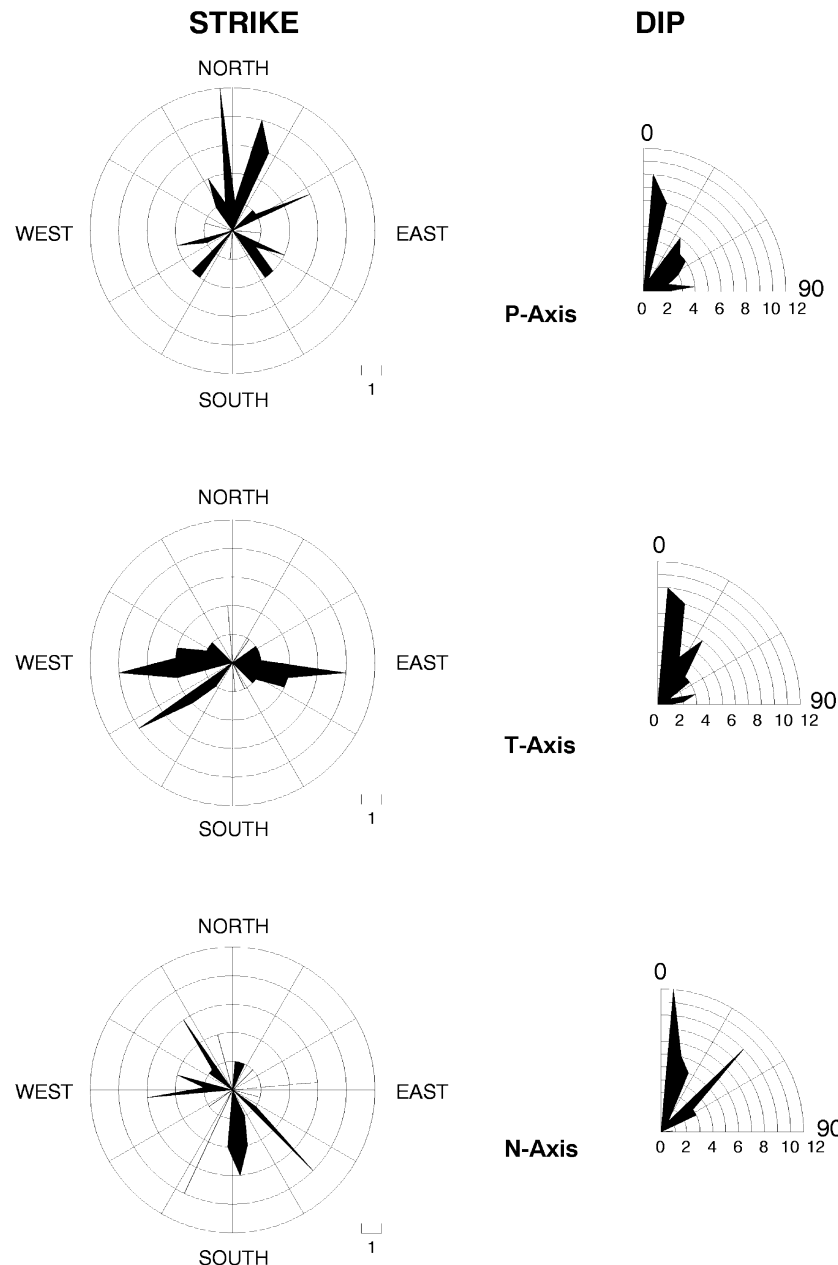
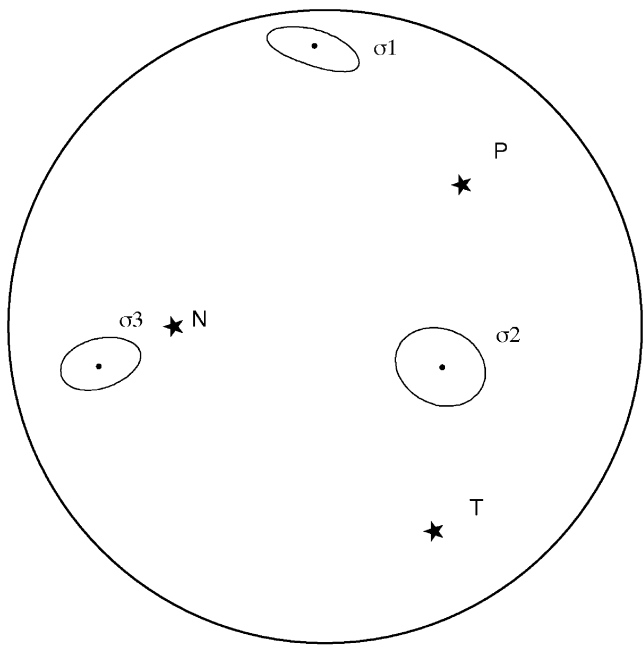


**Figure 8.** Normalized rose diagrams of P-, T- and N-axes from the 39 fault-plane solutions determined. The angular bin size is 15°.

Most of the aftershocks are located on the concave (north) side of the fault system. To elucidate the mechanism of this complex fault geometry and to explain the aftershock distribution, we modelled the coseismic stress change using the Dis3D code (Erickson 1987). This program calculates in three dimensions the displacements, tilts, strains and stresses due to motions on dislocations in an elastic half-space. The main shock was interpreted as a  $N96^\circ E \pm 5^\circ$  left-lateral strike-slip event with local magnitude ( $M_L$ ) 5.2 (Rigo *et al.* 1997). The main-shock depth was  $7.7 \pm 2.5$  km. First, we modelled the main shock with a single fault segment striking  $N96^\circ E$ , 4.5 km long and 5 km wide with the lower edge of the dislocation at 10 km depth. Then, for consistency with the magnitude, we imposed 8 cm of left-lateral slip according to the standard scaling laws (Hanks & Kanamori 1979). In a second model, we took into account the geological geometry of the faults, with

three vertical dislocations: a  $N120^\circ E$ -striking fault segment 2 km long, a  $N105^\circ E$ -striking fault segment 2.5 km long and a  $N85^\circ E$ -striking fault segment 2 km long, each fault segment being 5 km wide. As in the first model, the lower edges of the dislocations were fixed at 10 km depth. We set left-lateral slips of 8, 8 and 1 cm, respectively, on these fault segments. The sum of the three fault elements produced a total moment of  $5.4 \times 10^{16}$  N m (assuming a shear modulus of 30 GPa), which is consistent with the observed main-shock magnitude. Furthermore, the average strike of  $N112^\circ E$  for the three-element model is in reasonable agreement with the strike of  $N96^\circ E \pm 5^\circ$  observed for the main-shock mechanism. More information about the propagation of this rupture is required to determine whether the slip on the third fault segment is related to the main shock or to the  $M_L = 4.0$  aftershock which occurred less than one hour after the main shock (the



Aftershocks	Dip(°)	Strike(°)	Main Shock	Dip(°)	Strike(°)
σ1	10	358	P	34	44
σ2	55	109	N	47	270
σ3	25	260	T	24	152

**Figure 9.** Principal axes ( $\sigma_1, \sigma_2, \sigma_3$ ) of the stress tensor obtained from the subset of the 15 best-recorded aftershocks using global inversion. The ellipses correspond to one standard deviation. Also shown are the P-, T- and N-axes of the main shock (stars). Lower-hemisphere equal-area projection is used.

February 18 event at 02:27; see Rigo *et al.* 1997). In fact, in the first case, the third left-lateral fault element may accommodate the 8 cm of left-lateral slip postulated on the two other segments forming a bend (King & Nabelek 1985). The slip on this fault can then reach 8 cm with the resulting magnitude and focal mechanism still being in agreement with observations. However, the left-lateral slip may also involve the  $M_L = 4.0$  aftershock previously mentioned. In this case the main shock is well modelled with 8 cm left-lateral slip on the first two dislocations, giving an overall strike of N112°E and a magnitude  $M_W$  of 5.1, while the  $M_L = 4.0$  aftershock imposes a 1 cm slip on the third fault segment. We choose this 1 cm slip value, which also explains the relatively less important aftershock activity around the third fault segment.

We computed the values of Coulomb failure stress changes according to eqs 12 and 13 of King *et al.* (1994) on optimally oriented faults. Optimum fault angles are determined from the stress field calculated by adding a regional stress field to that created by the dislocation. We then calculated the Coulomb failure stress change,  $\sigma_f = \tau - \mu' \sigma_n$ , where  $\sigma_n$  and  $\tau$  are the normal and shear stresses and  $\mu'$  is the effective friction coefficient. The optimal fault orientations are mainly set by the regional stress direction, which is the most influential parameter in this kind of model (King *et al.* 1994). Following the previous discussion, we have considered the regional stress to be a simple horizontal compression ( $S_H$ ); considering the rupture mechanism, this component will have an influence on

the stress field following the main shock that is much larger than the other two components. As its possible orientation and amplitude are both uncertain, owing to a poor knowledge of the regional tectonic context, we have checked orientation values from N15°E to N55°E, a range which includes the main-shock P-axis, and two stress values, 10 and 3 MPa. From this model, it turns out that the regional stress field orientation is rather well constrained by the observations: the aftershock distribution pattern is best explained for an orientation of N30°E ± 10° (Fig. 10). By contrast, the stress value is poorly constrained: for the two stress values, the overall pattern of the Coulomb failure stress change field is nearly the same. This is a consequence of the low magnitude of the main shock, which hardly perturbs the pre-existing regional field. The lowest value of 3 MPa allows the generation of small variations in the fault-plane optimal orientations, in particular in the vicinity of the three fault segments (Fig. 10).  $\mu'$  is also a rather insensitive parameter (King *et al.* 1994). In our case, a high  $\mu'$  value increases the size of the fault-end lobes of positive Coulomb failure stress change. We choose a value of 0.4, which gives the best correlation between aftershock distribution and the pattern of Coulomb failure stress changes. Fig. 10 shows the Coulomb failure stress change and the optimum right-lateral and left-lateral slip planes, at 7.5 km depth, for a regional stress field of 3 MPa oriented N30°E and  $\mu' = 0.4$ . Superimposed are the aftershock locations and the focal mechanisms for the two models. In Fig. 10(a), modelling the main shock with a single fault plane seems too simple to explain the aftershock distribution. The features of the Coulomb failure stress do not fit the aftershock distribution very well, particularly in the NW part of the fault. With the three-fault model (Fig. 10b), most of the aftershocks concentrate where the predicted Coulomb failure stress increases by more than 0.2 MPa. Thus, this simple model provides a fairly successful explanation of the aftershock distribution. We note in addition that when the field induced by the main shock is superimposed on the regional field, the resulting compression axis in the vicinity of the three fault segments is not very different to that previously inferred from the aftershock first-motion analysis.

Beyond the fault ends, aftershock activity is less intense and is not well explained by the model—some events fall where the predicted Coulomb failure stress decreases, whereas areas where the Coulomb failure stress increases are aseismic. This lack of activity beyond the fault end may be an artefact due to the absence of the events unrecorded during the first 30 hr following the main shock. It may also be a consequence of edge effects near the fault ends. We investigated a model in which a left-lateral slip of 8 cm occurs on the third fault segment. It appears less successful because it increases the aseismic areas in regions of large Coulomb failure stress change. This result favours a rupture of the southern fault segment during the large aftershock, which occurred 1 hr after the main shock.

Small-magnitudes aftershocks ( $M_L \leq 3$ ), which correspond to small source radii, may occur on major faults or on small fractures, which are often observed in the vicinity of fault planes (Chester & Logan 1986; Scholz 1990). The diversity of the focal mechanisms observed in the Agly seismic crisis may be explained by activity not only on major faults but also on small fractures through a volume of rock of the order of a few tens of cubic kilometres in the vicinity of the fault bend. However, we note that the great diversity in strike shown by

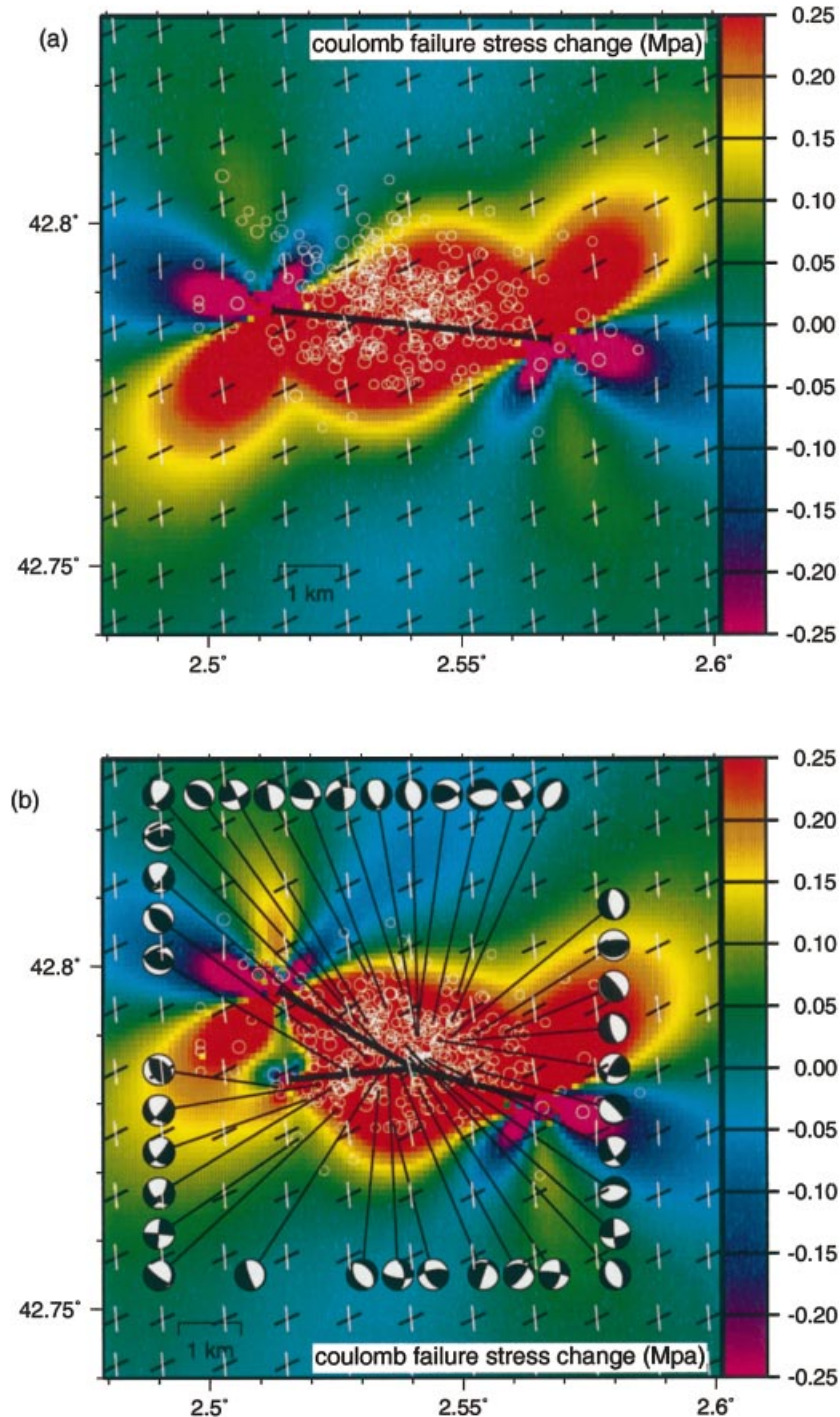


**Figure 10.** Coulomb failure stress changes, at 7.5 km depth, caused by the 1996 February 18  $M_L = 5.2$  earthquake. The regional stress  $S_H$  has an amplitude of 3 MPa and is oriented N30°E. The effective coefficient of friction  $\mu'$  is 0.4. Optimum right-lateral (white) and left-lateral (black) slip planes, aftershock epicentral locations and fault-plane solutions are superimposed. (a) One-fault model, 4.5 km long and 5 km wide with 8 cm of left-lateral slip. (b) Three-fault model, 5 km wide with left-lateral slip for a total moment of  $5.4 \times 10^{16}$  N m (see text for details).

the aftershock focal mechanisms may not be explained by the previous model (Fig. 10b). Even with the low (3 MPa) regional stress field we considered, the slip planes predicted by the model do not vary strongly inside the volume where the Coulomb failure stress change is at a maximum. It would be necessary to consider a very low regional stress field, on the same order as the stress drop during rupture (approximately 0.3 MPa) in

order to obtain highly variable fault-plane directions. Such values are unrealistically low: hydraulic fracturing experiments at 9 km depth in south Germany revealed a horizontal stress larger than 180 MPa (KTB experiment, Brudy *et al.* 1997); on the other hand, indirect measurements at the San Andreas fault and other places resulted in values of the order of 10–20 MPa (Hickman 1991; Lachenbruch & Sass 1992).

For the Agly crisis, the great diversity of focal mechanisms is probably related to the existence of pre-existing faults with various orientations. On the geological maps (e.g. Delay 1989), numerous small faults with various orientations are reported, in addition to the major faults oriented N110°E. A similar complexity is probably present at depth. An inconsistency between fault-plane solutions and model predictions has also been observed for the Loma Prieta aftershock sequence (Beroza & Zoback 1993; Kilb *et al.* 1997). A decrease in fault strength induced by pore-pressure variations has been invoked as a possible mechanism controlling earthquake occurrence, explaining the diversity in fault-plane solutions (Beroza & Zoback 1993). Intense fluid circulation is likely to be present in the Agly massif: hydrological perturbations were observed before and after the main shock, with temperature increases, gas emanations and appearance of new springs. Changes in water reservoir compositions have also been observed (Toutain *et al.* 1997). They could play an important role in modifying fault strength, making the triggering of aftershocks with unfavourable fault orientations possible.

## 6 CONCLUSIONS

Less than 36 hr after the magnitude  $M_L = 5.2$  Saint-Paul de Fenouillet earthquake, a temporary network of portable seismological stations was installed. More than 1200 events were recorded during four days, 336 of which could be accurately located. Fault-plane solutions were determined for 39 of these

events. They exhibit a rather large diversity, with reverse, normal and strike-slip mechanisms. A careful analysis of these events has allowed us to understand the earthquake rupture better and the aftershocks in the tectonic context.

The main shock most probably occurred on the Saint-Arnac Fault (SAF), a vertical fault with a complex geometry of three segments with different strikes (N120°E, N105°E and N85°E) forming a three-fault junction. Near this junction, aftershocks occurred between 5 and 11 km depth. Consequently, we infer that the fault mapped at the surface in the Agly massif (Delay 1989) extends down to at least 11 km depth (Fig. 11). This depth probably corresponds to the limit between the brittle upper crust and the ductile lower crust. This result is consistent with the geological setting of the Agly massif, which is a granitic unit intruded into the North Pyrenean Frontal Thrust after Cretaceous time (Fig. 11).

The main event caused the stress field amplitude and orientation to change locally. Calculation of the post-earthquake Coulomb failure stress changes on optimally oriented faults provides a successful explanation of the aftershock distribution: 90 per cent of the aftershocks occurred where modelled Coulomb failure stress increased by more than 0.2 MPa. A regional stress field with horizontal compression oriented N30°E ± 10° is favoured by the model. However, the inability of this model to predict the great diversity of the aftershock focal mechanisms suggests that these events occurred on pre-existing faults, and that their triggering may have been partly controlled by a decrease in fault strengths due to the presence of fluids in the crust.

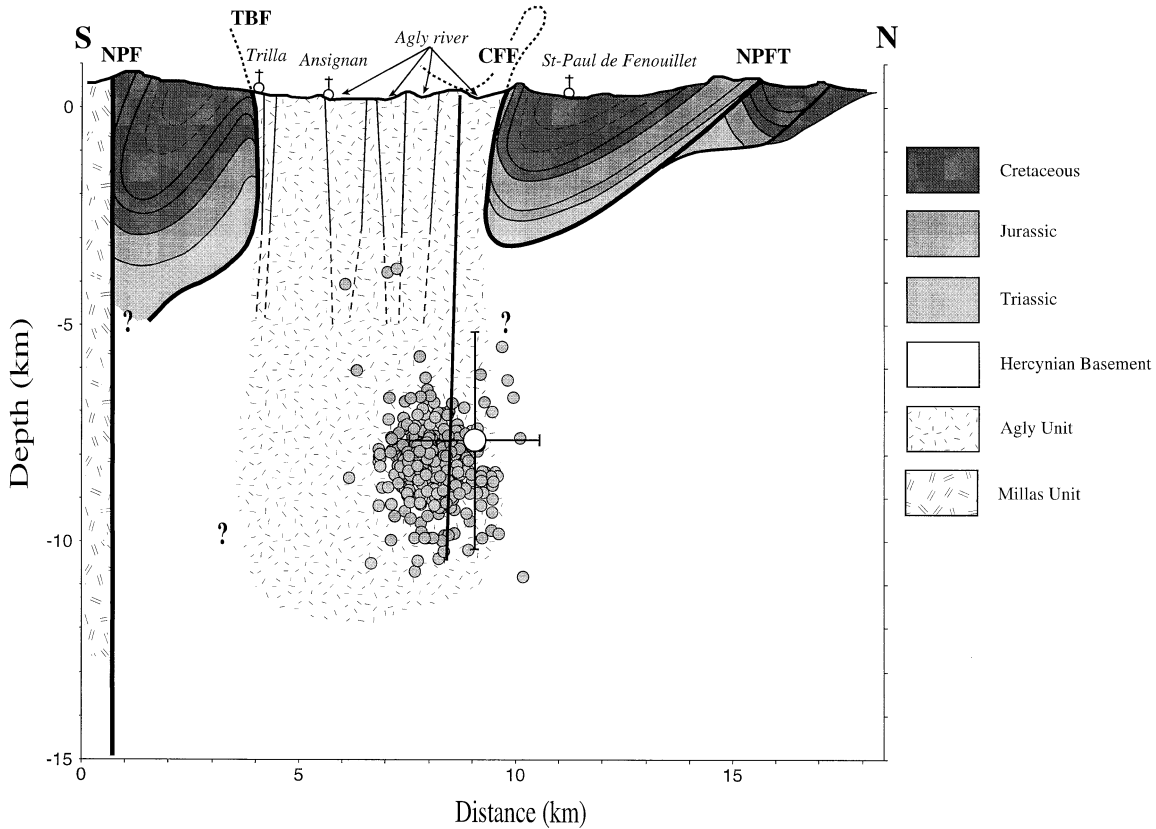


**Figure 11.** N–S geological cross-section across the Agly massif. No vertical exaggeration. All hypocentres of this study are projected onto the vertical plane. White circle with location error bars represents the main shock. N.P.F.: North Pyrenean Fault; T.B.F.: Trilla–Belest Fault; C.F.F.: Clue-de-la-Fou Fault; N.P.F.T.: North Pyrenean Frontal Thrust.

The major earthquakes that occurred in the eastern French Pyrenees prior to 1996 could be ascribed to one of three major faults which are well documented in that part of the range: the North Pyrenean Fault, the North Pyrenean Frontal Thrust and the Tet Fault. Prior to the 1996 earthquake, the Saint-Arnac Fault appeared on geological maps, but it had never been considered as an active fault. This fault was probably reactivated because of its favourable orientation in relation to the regional-stress-field orientation. This illustrates how difficult it is to evaluate the seismic risk precisely, even in an area of moderate seismicity where historical seismicity is well documented. It also shows the importance of maintaining seismological networks for several decades in order to obtain reliable catalogues of instrumental seismicity.

## ACKNOWLEDGMENTS

We thank the RENASS (Strasbourg) and the LGIT-IRIGM (Grenoble) for lending us seismographic stations, and the participants of the post-earthquake field experiment. We also thank the Mayor's staff in Saint-Paul de Fenouillet for their logistic support. We thank A. Gresillaud for his phase pickings and the Servei Geològic de Catalunya for generously providing their data. We also thank the two reviewers, Prof. Daignières and Dr Amato for their constructive comments. K. Feigl helped to improve the manuscript. This work was supported by the 'Programme National Risques Naturels' from the French Institut National des Sciences de l'Univers (CNRS/INSU).

## REFERENCES

- Armijo, R., Carey, E. & Cisternas, A., 1982. The inverse problem in microtectonics and the separation of tectonic phases, *Tectonophysics*, **82**, 145–160.
- Beroza, G.C. & Zoback, M.D., 1993. Mechanism diversity of the Loma Prieta aftershocks and the mechanisms of mainshock–aftershock interaction, *Science*, **259**, 210–213.
- Braigis, A., Armijo, R., Winter, T., Tapponnier, P. & Hebbecq, A., 1990. Morphological evidence for Quaternary normal faulting and seismic hazard in the Eastern Pyrenees, *Ann. Tectonicae*, **IV**(1), 19–42.
- Brudy, M., Zoback, M.D., Fuchs, K., Rummel, F. & Baumgärtner, J., 1997. Estimation of the complete stress tensor to 8 km depth in the KTB scientific drill holes: implications for crustal strength, *J. geophys. Res.*, **102**, 18 453–18 475.
- Cadiot, B., Delaunay, J. & Vogt, J., 1979. Tableaux anthologiques de la sismicité de la France, in *Les Tremblements de Terre En France*, Vol. 96, pp. 17–152, ed. Vogt, J., Éditions Du Bureau de Recherche Géologiques et Minières.
- Chester, F.M. & Logan, J.M., 1986. Implications for mechanical properties of brittle faults from observations of the Punchbowl fault zone, California, *Pageoph.*, **124**, 79–106.
- Choukroune, P., 1992. Tectonic evolution of the Pyrenees, *Ann. Rev. Earth planet. Lett.*, **20**, 143–158.
- Choukroune, P. & ECORS team, 1989. The ECORS Pyrenean deep seismic profile reflection data and the overall structure of an orogenic belt, *Tectonics*, **8**, 23–29.
- Choukroune, P., Roure, F., Pinet, B. & ECORS Pyrenees team, 1990. Main results of the ECORS Pyrenees profile, *Tectonophysics*, **173**, 411–423.
- Correig, A.M., Urquizú, M. & Vila, J., 1997. Aftershock series of event February 18, 1996: an interpretation in terms of self-organized criticality, *J. geophys. Res.*, **102**, 27 407–27 420.
- Daignières, M., Gallart, J., Banda, E. & Hirn, A., 1982. Implications of the seismic structure for the orogenic evolution of the Pyrenees range, *Earth planet. Sci. Lett.*, **57**, 88–100.
- Das, S. & Scholz, C., 1981. Off-fault aftershock clusters caused by shear stress increase?, *Bull. seism. Soc. Am.*, **71**, 1669–1675.
- Delay, F., 1989. Le massif Nord-Pyrénéen de l'Agl (Pyrénées Orientales): évolution tectono-métamorphique et exemple d'un amincissement crustal polyphasé, *Thèse De Doctorat*, Université de Lille, France.
- ECORS Pyrenees Team, 1988. The deep reflection seismic survey across the Pyrenees, *Nature*, **331**, 508–511.
- Erickson, L., 1987. *User's manual for DIS3D: a three-dimensional dislocation program with applications to faulting in the earth*, Stanford University, Stanford, CA.
- Fonteilles, M., 1970. Géologie des terrains métamorphiques du massif hercynien de l'Agl (Pyrénées Orientales), *Bull. Bureau de Recherche Géologiques et Minières*, **4**, 21–72.
- Gagnepain, J., Modiano, T., Cisternas, A., Ruegg, J.C., Vadell, M., Hatzfeld, D. & Mezcua, J., 1980. Sismicité de la région d'Arette (Pyrénées-Atlantiques) et mécanismes au foyer, *Ann. Geophys.*, **36**, 499–508.
- Gagnepain-Beyneix, J., Haessler, H. & Modiano, T., 1982. The pyrenean earthquake of February 29, 1980: an example of complex faulting, *Tectonophysics*, **85**, 273–290.
- Gagnepain-Beyneix, J., Massinon, B., Olivera, C. & Martinez-Solarès, J.M., 1997. Sismicité de la chaîne des Pyrénées et ses avant-pays, in *Synthèse Géologique des Pyrénées*, Bur. Rech. Géol. Min., Orléans, France, in press.
- Gallart, J., Daignières, M., Banda, E., Suriñach, E. & Hirn, A., 1980. The Eastern Pyrenean domain: lateral variations at crustal-mantle level, *Ann. Geophys.*, **36**, 141–158.
- Gallart, J., Banda, E. & Daignières, M., 1981. Crustal structure of the Paleozoic Axial Zone of the Pyrenees and transition to the North Pyrenean Zone, *Ann. Geophys.*, **37**, 457–480.
- Gallart, J., Olivera, C., Daignières, M. & Hirn, A., 1982. Quelques données récentes sur la relation entre fractures crustales et séismes dans les Pyrénées Orientales, *Bull. Soc. Géol. Fr.*, **24**, 293–298.
- Hanks, T.C. & Kanamori, H., 1979. A moment magnitude scale, *J. geophys. Res.*, **84**, 2348–2350.
- Hauksson, E., 1994. State of stress from focal mechanisms before and after the 1992 Landers earthquake sequence, *Bull. seism. Soc. Am.*, **84**, 917–934.
- Hickman, S.H., 1991. Stress in the Lithosphere and the strength of active faults, *Rev. Geophysics*, Suppl., 759–775.
- Hirn, A., Daignières, M., Gallart, J. & Vadell, M., 1980. Explosion seismic sounding of throws and dips in the continental moho, *Geophys. Res. Lett.*, **7**, 263–266.
- Kilb, D., Ellis, M., Gomberg, J. & Davis, S., 1997. On the origin of diverse aftershock mechanisms following the 1989 Loma Prieta earthquake, *Geophys. J. Int.*, **128**, 557–570.
- King, G.C.P. & Nabelek, J., 1985. Role of fault bends in the initiation and termination of earthquake rupture, *Science*, **228**, 984–987.
- King, G.C.P., Stein, R.S. & Lin, J., 1994. Static stress changes and the triggering of earthquakes, *Bull. seism. Soc. Am.*, **84**, 935–953.
- Lachenbruch, A.H. & Sass, J.H., 1992. Heat flow from Cajon Pass, fault strength, and tectonic implications, *J. geophys. Res.*, **97**, 4995–5015.
- Lambert, J. & Levret-Albaret, A., 1996. *Mille Ans de Séismes en France, Ouest* Éditions, Bureau de Recherches Géologiques et Minières, Électricité de France, Institut de Protection et de Sureté Nucléaire.
- Lee, W.H.K. & Lahr, J.C., 1975. HYPOT1 (revised): a computer program for determining hypocenter, magnitude and first motion pattern of local earthquakes, *USGS Open-File Rept.*, 75–311.
- Mattauer, M., 1990. Une autre interprétation du profil ECORS Pyrénées, *Bull. Soc. Géol. Fr.*, **6**, 307–311.
- Njike Kassala, J.D., Souriau, A., Gagnepain-Beyneix, J., Martel, L. & Vadell, M., 1992. Frequency-magnitude relationship and Poisson's ratio in the Pyrenees, in relation to earthquake distribution, *Tectonophysics*, **215**, 363–369.

- Olivera, C., Gallart, J., Goula, X. & Banda, E., 1986. Recent activity and seismotectonics of the eastern Pyrenees, *Tectonophysics*, **129**, 367–380.
- Philip, H., Bousquet, J.C., Escuer, J., Fleta, J., Goula, X. & Grellet, B., 1992. Présence de failles inverses d'âge quaternaire dans l'Est des Pyrénées: implications sismotectoniques, *C. R. Acad. Sci. Paris*, **314**, Série II, 1239–1245.
- Puigdefabregas, C. & Souquet, P., 1986. Tecto-sedimentary cycles and depositional sequences of the Mesozoic and Tertiary from the Pyrenees, *Tectonophysics*, **129**, 173–203.
- Rehaut, J.P., Boillot, G. & Mauffret, A., 1984. The Western Mediterranean Basin geological evolution, *Mar. Geol.*, **55**, 447–477.
- Rigo, A., Pauchet, H., Souriau, A., Grésillaud, A., Nicolas, M., Olivera, C. & Figueras, S., 1997. The February 1996 earthquake sequence in the eastern Pyrenees: first results, *J. Seism.*, **1**, 3–14.
- Rivera, L. & Cisternas, A., 1990. Stress tensor and fault plane solutions for a population of earthquakes, *Bull. seism. Soc. Am.*, **80**, 600–614.
- Scholz, C.H., 1990. *The Mechanics of Earthquakes and Faulting*, Cambridge University Press, Cambridge.
- Souriau, A. & Granet, M., 1995. A tomographic study of the lithosphere beneath the Pyrenees from local and teleseismic data, *J. geophys. Res.*, **100**, 18117–18134.
- Souriau, A. & Pauchet, H., 1998. A new synthesis of the Pyrenean seismicity and its tectonic implications, *Tectonophysics*, **290**, 221–244.
- Stein, R.S. & Lisowski, M., 1983. The 1979 Homestead valley earthquake sequence, California: control of aftershock and post-seismic deformation, *J. geophys. Res.*, **88**, 6477–6490.
- Suriñach, E., Marthelot, J.M., Gallart, J., Daignières, M. & Hirn, A., 1993. Seismic images and the evolution of the Iberian crust in the Pyrenees, *Tectonophysics*, **221**, 67–80.
- Toutain, J.P., Muñoz, M., Poitrasson, F. & Lienard, A.C., 1997. Springwater chloride ion anomaly prior to a  $M_I = 5.2$  earthquake, *Earth planet. Sci. Lett.*, **149**, 113–119.

## APPENDIX A

Event locations from HYPO71. rms: root mean square of the computed location; ERH: precision on the epicentral position; ERZ: precision on the focal depth; Q: quality output from HYPO71; n.ph.: Number of phases used for the location.

No.	Date yymmdd	Time hh:mm:ss	Latitude °N	Longitude °E	Depth km	$M_I$	rms s	ERH km	ERZ km	Q	n.ph.
1	960219	8:34:36.84	42°48.41	2°30.17	10.91	3.47	0.20	2.9	2.5	C	6
2	960219	10:18:56.79	42°46.59	2°31.56	8.09	2.08	0.05	0.9	0.7	B	6
3	960219	10:20:12.42	42°46.59	2°32.11	8.22	2.40	0.02	0.4	0.3	B	6
4	960219	10:54:53.07	42°47.73	2°33.23	10.28	3.44	0.27	1.3	1.3	C	14
5	960219	12:05:28.54	42°47.05	2°31.71	8.46	3.23	0.05	0.6	0.5	B	8
6	960219	12:15:21.19	42°46.97	2°32.46	8.25	3.03	0.05	1.1	0.6	C	7
7	960219	12:17:13.43	42°46.76	2°32.58	7.95	3.42	0.06	1.1	0.7	C	7
8	960219	12:25:28.28	42°47.38	2°31.74	8.01	3.26	0.07	1.3	0.8	C	7
9	960219	13:10:51.14	42°47.06	2°34.77	10.78	3.64	0.29	1.4	1.6	B	17
10	960219	13:49:40.19	42°46.90	2°32.59	8.45	2.74	0.09	0.9	0.7	B	9
11	960219	13:51:03.96	42°46.86	2°31.87	8.59	3.07	0.06	1.1	0.6	C	7
12	960219	14:03:09.94	42°47.58	2°32.99	8.63	2.46	0.03	0.5	0.4	B	7
13	960219	14:13:24.30	42°47.88	2°32.77	6.16	2.62	0.20	2.2	2.1	B	8
14	960219	14:32:30.07	42°46.81	2°31.54	7.94	2.81	0.07	0.9	0.7	B	8
15	960219	14:40:55.21	42°47.84	2°32.01	7.97	2.37	0.06	0.7	0.7	B	6
16	960219	14:44:55.46	42°46.61	2°32.18	8.13	3.11	0.07	0.5	0.4	B	12
17	960219	14:57:09.59	42°46.81	2°32.26	8.56	2.70	0.08	0.6	0.6	B	10
18	960219	15:28:17.54	42°46.21	2°31.35	8.59	2.64	0.07	0.5	0.5	B	10
19	960219	15:29:50.70	42°46.59	2°31.96	7.92	2.42	0.03	0.4	0.3	B	7
20	960219	15:31:54.26	42°47.42	2°31.99	8.23	2.93	0.14	1.5	1.1	B	9
21	960219	15:39:01.52	42°46.88	2°31.92	8.25	2.76	0.08	0.5	0.5	A	12
22	960219	15:51:22.40	42°46.31	2°31.70	6.07	2.61	0.05	0.5	0.6	B	9
23	960219	16:04:22.76	42°47.35	2°32.71	10.48	3.82	0.32	0.8	1.2	B	28
24	960219	16:03:54.53	42°47.19	2°32.53	8.20	2.49	0.14	0.7	1.0	B	11
25	960219	16:07:33.09	42°47.48	2°31.62	7.57	2.82	0.09	0.4	0.7	B	11
26	960219	16:11:27.49	42°47.00	2°32.85	7.38	2.63	0.09	0.6	1.0	B	8
27	960219	16:12:55.02	42°47.73	2°32.28	8.43	2.51	0.10	0.7	0.8	B	9
28	960219	17:18:40.57	42°47.47	2°31.58	8.49	3.67	0.16	0.7	1.0	B	12
29	960219	17:20:00.57	42°47.52	2°30.95	8.32	2.71	0.10	0.6	0.8	B	9
30	960219	17:20:27.72	42°46.81	2°31.28	8.09	2.53	0.08	0.4	0.5	B	12
31	960219	17:24:05.67	42°47.17	2°32.45	8.34	2.30	0.07	0.7	1.1	B	6
32	960219	17:35:21.11	42°47.60	2°32.07	8.01	2.55	0.08	0.7	1.1	B	6
33	960219	17:49:11.64	42°47.10	2°31.59	7.97	2.90	0.18	0.8	1.3	B	13
34	960219	17:49:34.06	42°47.53	2°32.65	9.08	3.40	0.34	1.0	1.5	B	22
35	960219	17:52:53.78	42°47.17	2°31.35	6.74	3.34	0.22	0.8	1.1	B	16
36	960219	17:54:01.23	42°47.32	2°31.42	8.48	3.80	0.10	0.4	0.5	B	14
37	960219	18:26:29.00	42°47.00	2°31.65	8.40	3.33	0.07	0.3	0.5	A	12
38	960219	18:36:51.96	42°47.13	2°31.63	8.09	2.80	0.14	0.7	1.3	B	9
39	960219	18:35:53.39	42°47.60	2°31.47	8.47	2.98	0.08	0.6	0.6	B	9
40	960219	19:01:02.78	42°47.27	2°31.98	8.59	2.74	0.11	0.6	0.8	B	10
41	960219	19:04:13.19	42°47.20	2°31.72	6.52	2.76	0.29	1.2	2.2	B	12

No.	Date yymmdd	Time hh:mm:ss	Latitude °N	Longitude °E	Depth km	Ml	rms s	ERH km	ERZ km	Q	n.ph.
42	960219	19:03:40.60	42°46.85	2°31.18	8.09	2.89	0.12	0.5	0.8	B	12
43	960219	19:14:49.02	42°47.40	2°32.17	8.74	2.58	0.06	1.4	0.9	C	6
44	960219	19:19:19.66	42°47.30	2°32.90	7.68	2.56	0.08	0.5	0.7	B	9
45	960219	19:25:30.31	42°47.93	2°30.87	8.46	3.11	0.12	0.9	1.1	B	8
46	960219	19:30:13.84	42°47.43	2°32.57	9.01	2.44	0.05	1.2	0.6	C	7
47	960219	19:54:36.69	42°47.40	2°33.73	8.17	2.52	0.07	1.2	0.7	C	8
48	960219	19:56:22.41	42°47.30	2°32.00	7.73	2.79	0.13	0.6	1.1	B	10
49	960219	19:59:34.43	42°47.12	2°32.08	8.07	2.74	0.15	0.7	1.1	B	11
50	960219	19:60:42.32	42°47.45	2°31.61	8.62	2.39	0.09	0.8	1.2	B	7
51	960219	20:06:24.74	42°47.54	2°30.50	9.34	2.85	0.12	1.0	0.9	B	9
52	960219	20:20:06.20	42°47.48	2°32.04	7.03	3.32	0.20	1.1	1.4	B	10
53	960219	20:25:18.20	42°47.75	2°32.94	9.60	3.81	0.32	0.8	1.2	B	30
54	960219	20:34:03.79	42°47.38	2°32.21	8.18	2.82	0.06	0.4	0.6	B	9
55	960219	20:40:42.77	42°47.30	2°31.81	7.61	3.17	0.12	0.5	0.8	A	12
56	960219	21:06:00.48	42°47.59	2°31.64	8.30	2.89	0.18	0.9	1.2	B	11
57	960219	21:14:26.59	42°47.41	2°33.15	8.98	3.67	0.37	1.1	1.4	B	23
58	960219	21:28:21.50	42°47.52	2°32.31	6.84	3.09	0.19	0.8	1.2	B	12
59	960219	22:05:57.64	42°47.58	2°31.89	7.34	3.27	0.20	0.7	1.2	B	14
60	960219	22:14:32.13	42°47.43	2°33.51	9.94	3.67	0.34	0.9	1.2	B	30
61	960219	22:22:11.83	42°47.67	2°32.06	6.94	2.73	0.18	0.7	1.2	B	11
62	960219	22:27:06.32	42°47.09	2°32.24	7.58	3.43	0.17	0.6	1.0	B	15
63	960219	22:50:17.99	42°47.18	2°31.53	7.65	2.41	0.13	1.5	2.4	B	6
64	960219	22:54:48.04	42°47.13	2°32.33	7.45	3.40	0.14	0.5	0.7	A	16
65	960219	22:56:33.08	42°47.13	2°32.16	7.35	3.11	0.18	0.7	1.1	B	14
66	960219	23:10:24.87	42°47.39	2°31.68	7.08	2.69	0.14	0.6	0.9	A	13
67	960219	23:14:11.76	42°47.47	2°31.95	7.79	2.90	0.04	0.3	0.4	B	8
68	960219	23:16:29.30	42°47.23	2°31.22	8.71	2.81	0.09	0.6	0.7	B	9
69	960219	23:28:53.79	42°47.70	2°31.28	8.18	2.96	0.12	0.6	0.7	B	12
70	960219	23:56:33.06	42°47.26	2°29.89	9.13	2.66	0.32	2.4	2.8	C	8
71	960220	0:06:06.90	42°47.35	2°33.02	9.43	3.58	0.34	0.9	1.2	B	27
72	960220	0:32:08.75	42°46.89	2°30.84	8.29	2.62	0.13	0.7	1.2	B	9
73	960220	1:01:19.90	42°47.22	2°32.64	8.07	2.68	0.06	0.4	0.6	B	9
74	960220	1:05:42.67	42°47.16	2°32.53	7.23	3.17	0.14	0.5	1.0	A	12
75	960220	1:15:09.03	42°47.90	2°31.08	8.44	2.68	0.10	0.7	1.0	B	8
76	960220	1:33:30.03	42°47.56	2°32.04	7.77	3.15	0.11	0.5	0.8	B	11
77	960220	1:45:26.81	42°47.51	2°32.86	8.07	2.87	0.06	0.3	0.4	B	11
78	960220	2:08:18.73	42°47.21	2°32.53	8.84	2.32	0.06	0.6	0.9	B	6
79	960220	2:10:37.36	42°47.76	2°32.13	7.49	3.23	0.16	0.6	1.0	B	13
80	960220	2:37:14.01	42°47.33	2°32.15	7.08	3.42	0.13	0.5	0.8	A	14
81	960220	2:43:46.48	42°46.92	2°31.97	6.80	2.56	0.13	1.0	1.8	B	7
82	960220	3:06:53.10	42°47.36	2°31.91	8.66	2.75	0.09	0.7	0.9	B	7
83	960220	3:13:30.93	42°46.70	2°32.37	3.76	2.85	0.34	2.0	2.1	C	10
84	960220	3:18:35.92	42°47.36	2°32.72	8.58	2.52	0.03	0.2	0.4	B	7
85	960220	3:54:26.06	42°47.05	2°30.76	8.26	3.10	0.09	0.7	0.7	B	9
86	960220	4:01:47.18	42°47.12	2°32.58	8.19	2.23	0.06	0.4	0.5	B	9
87	960220	4:11:59.55	42°47.11	2°32.36	7.23	3.00	0.08	0.5	0.6	B	10
88	960220	4:23:01.68	42°47.93	2°32.24	6.81	3.09	0.21	0.9	1.2	B	13
89	960220	4:24:44.67	42°47.19	2°34.44	6.24	3.02	0.13	2.3	2.0	C	8
90	960220	4:40:11.60	42°47.76	2°31.12	8.71	2.85	0.09	0.8	1.0	B	7
91	960220	4:50:32.96	42°47.47	2°33.66	8.83	2.27	0.07	1.7	1.0	C	6
92	960220	4:51:04.38	42°47.61	2°31.30	7.48	3.03	0.15	0.8	1.0	B	11
93	960220	4:56:20.80	42°47.26	2°32.41	7.88	3.12	0.18	1.0	1.2	B	11
94	960220	4:60:11.49	42°47.73	2°31.82	8.06	3.07	0.16	0.9	1.2	B	10
95	960220	5:03:45.34	42°47.34	2°31.97	7.06	3.33	0.15	0.5	0.8	A	14
96	960220	5:09:45.39	42°47.93	2°30.58	8.72	3.20	0.14	0.9	0.9	B	9
97	960220	5:10:12.87	42°47.78	2°31.14	8.73	3.42	0.12	0.8	0.8	B	9
98	960220	5:17:28.22	42°46.94	2°31.90	8.44	3.19	0.09	0.5	0.6	B	11
99	960220	6:10:50.75	42°47.75	2°31.88	7.74	3.10	0.16	0.8	0.9	B	12
100	960220	6:14:32.09	42°47.58	2°32.35	7.88	2.76	0.13	2.4	1.1	C	8
101	960220	6:16:04.89	42°47.51	2°31.81	8.02	2.76	0.07	0.5	0.5	B	10
102	960220	6:31:21.39	42°46.92	2°32.48	9.37	3.44	0.22	0.6	1.0	B	22
103	960220	6:41:47.60	42°48.06	2°30.87	8.46	2.27	0.13	1.1	1.3	C	7
104	960220	6:53:17.30	42°46.92	2°32.45	7.90	3.17	0.19	0.8	1.2	B	13

No.	Date yymmdd	Time hh:mm:ss	Latitude °N	Longitude °E	Depth km	Ml	rms s	ERH km	ERZ km	Q	n.ph.
105	960220	6:59:12.31	42°47.31	2°32.89	8.41	3.16	0.10	1.4	0.7	C	10
106	960220	7:02:30.07	42°46.95	2°31.93	7.82	3.05	0.11	0.8	1.0	B	9
107	960220	7:04:01.08	42°46.89	2°31.88	8.11	3.36	0.17	0.7	1.2	B	12
108	960220	7:47:29.18	42°47.38	2°32.37	7.32	2.56	0.09	0.8	1.3	B	7
109	960220	8:02:01.93	42°46.91	2°34.17	7.19	2.94	0.02	0.7	0.4	B	6
110	960220	8:49:08.25	42°46.99	2°31.78	8.94	0.00	0.09	0.4	0.6	A	12
111	960220	8:49:15.61	42°46.93	2°31.54	8.77	3.19	0.06	0.3	0.5	B	10
112	960220	8:55:43.88	42°47.40	2°32.88	9.29	3.33	0.29	0.8	1.1	B	25
113	960220	8:57:25.02	42°47.40	2°31.94	7.76	2.83	0.13	0.6	1.0	B	10
114	960220	9:01:40.60	42°47.44	2°32.67	8.93	2.90	0.06	0.8	0.4	B	10
115	960220	9:05:56.19	42°46.86	2°31.24	8.71	3.32	0.11	0.4	0.5	A	17
116	960220	9:20:19.87	42°46.95	2°31.64	9.00	2.66	0.06	1.1	0.6	C	7
117	960220	9:20:44.11	42°46.97	2°32.74	7.91	2.61	0.06	1.0	0.6	C	8
118	960220	9:20:54.01	42°46.94	2°32.77	8.08	2.90	0.08	1.0	0.6	C	10
119	960220	9:22:23.35	42°47.08	2°31.63	10.53	3.63	0.28	0.6	1.0	B	32
120	960220	9:23:33.85	42°47.36	2°32.73	9.29	2.08	0.16	0.9	1.3	B	11
121	960220	9:33:38.39	42°46.91	2°32.05	8.55	2.75	0.07	1.3	0.8	C	7
122	960220	10:21:57.65	42°47.01	2°31.47	8.34	2.82	0.04	0.3	0.6	B	8
123	960220	11:21:21.66	42°47.91	2°31.88	8.94	3.67	0.35	1.0	1.4	B	27
124	960220	11:30:43.79	42°47.30	2°30.35	9.03	3.03	0.14	2.0	1.3	C	8
125	960220	12:27:11.96	42°47.54	2°33.35	8.64	3.12	0.11	0.8	0.8	B	11
126	960220	12:33:36.18	42°47.37	2°32.15	9.15	2.62	0.04	0.5	0.5	B	7
127	960220	12:34:16.22	42°46.95	2°30.79	8.78	3.06	0.12	0.7	0.8	B	11
128	960220	12:36:13.88	42°46.83	2°32.06	8.31	2.54	0.05	0.9	0.5	B	7
129	960220	12:44:34.26	42°46.75	2°32.60	7.64	2.61	0.08	1.5	1.0	C	7
130	960220	12:58:30.07	42°47.12	2°32.11	9.64	3.92	0.26	0.7	1.1	B	29
131	960220	13:06:39.26	42°47.26	2°33.68	7.65	2.72	0.08	1.9	1.2	C	6
132	960220	13:08:21.01	42°47.56	2°31.52	7.48	3.14	0.15	0.7	0.9	A	13
133	960220	13:11:13.27	42°46.60	2°32.45	8.03	2.92	0.06	0.9	0.7	B	7
134	960220	13:13:26.45	42°47.22	2°31.64	7.96	3.12	0.12	0.9	1.1	B	8
135	960220	14:03:42.59	42°46.80	2°34.64	8.52	3.13	0.18	1.2	1.4	B	11
136	960220	14:27:27.52	42°47.31	2°31.87	7.96	3.36	0.38	1.0	1.3	B	25
137	960220	14:29:35.71	42°47.84	2°34.56	7.71	2.55	0.09	0.8	1.0	B	9
138	960220	14:42:08.30	42°47.86	2°31.95	7.83	2.97	0.14	1.0	1.0	B	10
139	960220	15:05:52.10	42°47.23	2°32.41	7.88	2.92	0.10	1.8	1.1	C	7
140	960220	15:13:10.81	42°47.63	2°31.64	8.81	3.39	0.29	0.8	1.2	B	27
141	960220	15:21:35.77	42°47.40	2°32.17	8.81	2.80	0.09	0.8	0.6	B	11
142	960220	15:27:28.00	42°46.49	2°31.04	10.59	3.30	0.36	1.1	1.5	B	25
143	960220	15:27:03.18	42°46.17	2°33.91	4.04	2.83	0.39	1.2	2.8	C	19
144	960220	15:37:27.79	42°47.76	2°32.15	7.83	3.14	0.15	0.6	0.9	A	14
145	960220	15:38:06.69	42°47.21	2°32.58	7.71	2.57	0.09	0.4	0.7	B	11
146	960220	15:44:35.92	42°47.41	2°31.76	9.00	2.57	0.10	0.7	0.7	B	10
147	960220	15:51:19.53	42°47.50	2°31.96	9.17	2.82	0.05	0.3	0.4	B	9
148	960220	16:11:02.36	42°47.54	2°32.40	8.29	2.58	0.07	0.4	0.6	B	10
149	960220	16:27:03.88	42°47.64	2°32.09	7.79	3.30	0.11	0.4	0.6	A	16
150	960220	16:32:36.54	42°46.93	2°31.43	8.35	2.81	0.15	0.5	0.7	B	19
151	960220	17:03:47.86	42°47.27	2°33.54	8.49	3.07	0.08	0.6	0.6	B	11
152	960220	17:18:26.37	42°46.89	2°35.10	8.80	2.72	0.37	2.1	2.9	C	11
153	960220	17:20:34.50	42°47.50	2°32.00	9.28	2.27	0.09	0.8	0.9	B	8
154	960220	17:20:49.59	42°47.19	2°31.87	8.73	3.10	0.12	0.5	0.6	A	16
155	960220	17:22:43.17	42°47.47	2°32.50	8.73	2.69	0.08	0.6	0.7	B	8
156	960220	17:29:03.23	42°47.05	2°32.86	8.17	2.59	0.09	1.3	1.3	C	7
157	960220	17:38:36.47	42°47.70	2°31.80	8.12	2.63	0.07	0.4	0.6	B	11
158	960220	17:45:10.12	42°46.92	2°31.59	8.53	2.40	0.06	0.4	0.6	B	8
159	960220	17:56:09.59	42°47.02	2°33.12	7.83	2.99	0.08	0.5	0.7	B	10
160	960220	18:09:55.18	42°46.94	2°33.36	7.44	2.49	0.05	0.7	0.8	B	7
161	960220	18:16:36.37	42°46.59	2°32.26	9.25	3.11	0.16	0.8	1.0	B	12
162	960220	18:21:33.48	42°47.55	2°31.95	8.05	2.98	0.12	0.6	0.9	B	11
163	960220	18:33:17.74	42°47.30	2°32.58	8.74	3.06	0.06	0.6	0.6	B	8
164	960220	18:44:22.17	42°47.14	2°33.25	7.49	2.81	0.03	0.4	0.5	B	7
165	960220	18:48:48.76	42°47.43	2°32.51	8.30	2.99	0.11	0.6	0.9	B	11
166	960220	18:56:22.78	42°46.61	2°32.49	8.32	2.55	0.08	1.6	1.0	C	7
167	960220	19:01:50.43	42°47.23	2°32.78	7.59	2.25	0.08	1.1	1.2	C	7

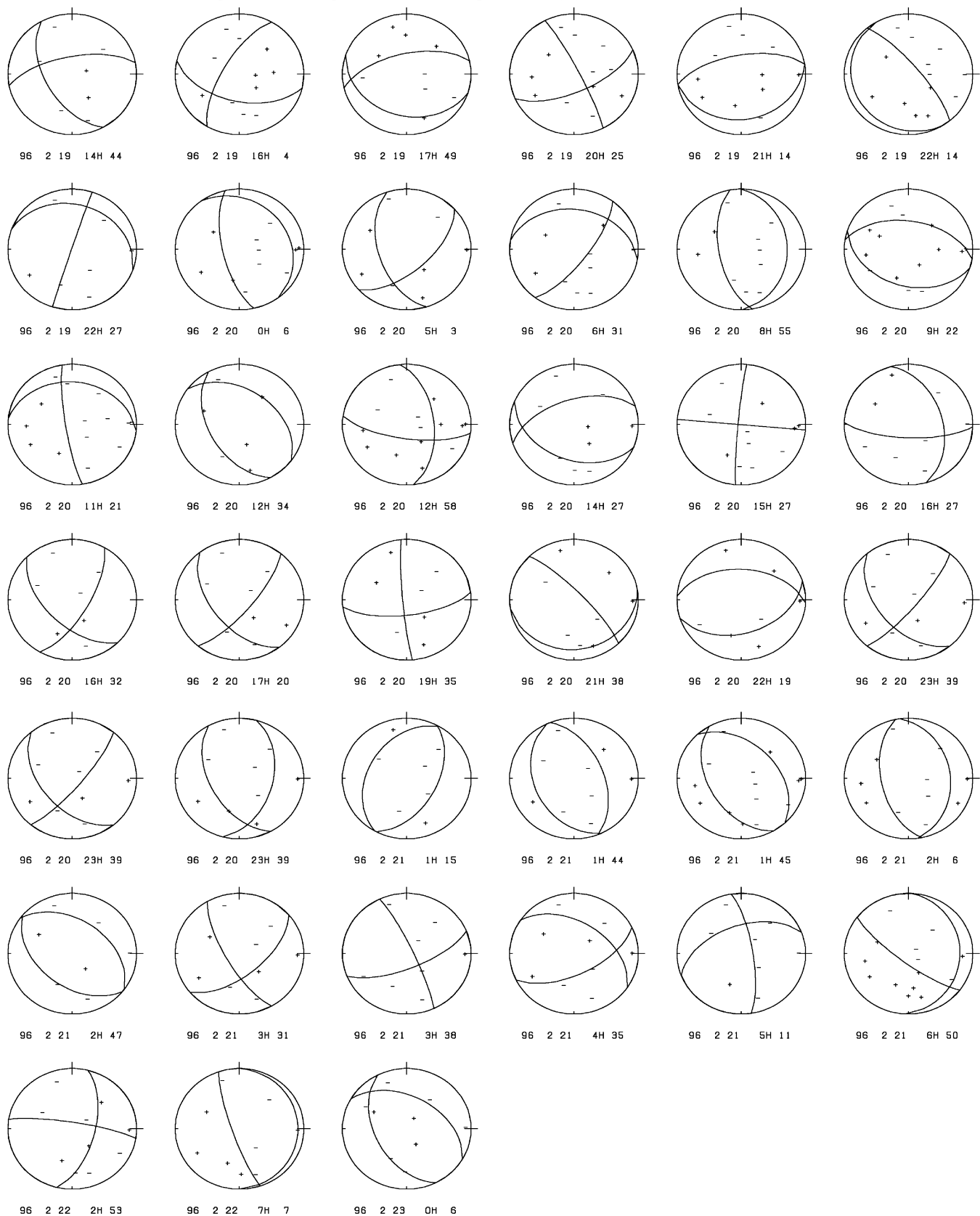
No.	Date yymmdd	Time hh:mm:ss	Latitude °N	Longitude °E	Depth km	Ml	rms s	ERH km	ERZ km	Q	n.ph.
168	960220	19:07:17.43	42°47.54	2°32.36	8.57	2.52	0.09	1.9	1.1	C	7
169	960220	19:11:10.62	42°47.34	2°32.96	8.46	3.26	0.09	0.4	0.7	B	12
170	960220	19:35:33.17	42°47.24	2°32.40	8.61	2.81	0.11	0.5	0.7	B	13
171	960220	19:55:47.32	42°47.56	2°32.02	8.46	2.80	0.16	0.6	0.9	B	14
172	960220	20:05:51.38	42°47.30	2°33.09	8.21	3.00	0.07	0.4	0.5	B	12
173	960220	20:07:16.44	42°47.13	2°32.63	9.86	2.95	0.31	1.3	1.8	B	14
174	960220	20:14:12.04	42°47.35	2°32.59	8.24	2.57	0.04	0.2	0.3	B	9
175	960220	20:22:08.05	42°47.12	2°33.69	7.77	3.11	0.12	0.8	0.8	B	12
176	960220	20:24:02.82	42°46.91	2°32.33	7.38	2.49	0.06	0.5	0.8	B	7
177	960220	20:25:12.24	42°47.43	2°32.34	7.62	2.52	0.07	1.4	0.8	C	7
178	960220	20:48:33.75	42°47.59	2°32.26	7.65	2.77	0.07	0.6	0.6	B	9
179	960220	20:51:37.37	42°47.11	2°31.47	8.98	2.83	0.11	0.7	0.7	B	10
180	960220	21:11:19.61	42°47.64	2°29.89	8.29	2.18	0.17	1.6	1.5	C	9
181	960220	21:38:07.75	42°47.09	2°33.19	7.95	3.32	0.18	0.6	0.9	B	20
182	960220	20:59:58.92	42°46.92	2°31.15	8.87	2.75	0.13	0.6	0.7	B	14
183	960220	22:11:21.59	42°47.62	2°32.79	8.51	2.37	0.10	1.5	1.4	C	7
184	960220	22:11:30.00	42°47.02	2°30.97	7.95	2.97	0.12	0.6	0.9	B	12
185	960220	22:15:22.80	42°47.40	2°31.41	8.29	2.85	0.10	0.7	0.9	B	8
186	960220	22:18:11.96	42°46.99	2°31.62	9.54	2.77	0.13	0.7	0.9	B	11
187	960220	22:19:17.74	42°47.60	2°31.83	7.89	2.32	0.12	0.7	0.9	B	10
188	960220	22:19:43.82	42°47.18	2°32.56	7.77	3.22	0.13	0.6	0.8	A	13
189	960220	22:23:56.28	42°47.02	2°33.36	7.63	2.77	0.06	0.5	0.6	B	9
190	960220	22:34:00.56	42°47.41	2°32.14	7.45	2.87	0.11	0.4	0.8	B	12
191	960220	22:53:23.56	42°46.91	2°31.56	8.17	2.72	0.04	0.2	0.3	B	11
192	960220	23:18:02.14	42°48.29	2°31.59	6.70	2.54	0.12	0.6	1.0	B	9
193	960220	23:22:41.04	42°47.29	2°33.05	6.82	3.30	0.17	0.5	0.9	B	19
194	960220	23:26:37.93	42°47.12	2°31.23	9.21	2.98	0.07	0.4	0.6	B	10
195	960220	23:38:01.18	42°48.22	2°32.29	6.30	2.51	0.20	0.7	1.2	B	12
196	960220	23:39:00.62	42°46.83	2°31.13	8.72	3.23	0.12	0.4	0.6	A	16
197	960220	23:39:28.27	42°46.97	2°31.28	8.88	2.81	0.12	0.4	0.6	A	18
198	960220	23:39:40.07	42°47.41	2°32.45	8.26	2.92	0.12	0.5	0.6	A	14
199	960221	0:01:56.72	42°47.36	2°32.26	8.54	2.51	0.14	0.7	1.0	A	13
200	960221	0:25:50.74	42°48.01	2°30.69	9.82	2.36	0.03	1.1	0.6	C	6
201	960221	0:34:00.12	42°47.63	2°31.75	7.85	2.25	0.04	0.4	0.5	B	7
202	960221	0:42:01.85	42°47.01	2°33.19	8.10	2.71	0.05	0.5	0.6	B	8
203	960221	0:43:10.13	42°47.24	2°31.68	6.66	2.97	0.17	0.7	1.2	B	13
204	960221	0:58:51.54	42°47.15	2°33.08	7.09	2.15	0.06	0.6	1.1	B	6
205	960221	0:59:18.84	42°47.17	2°32.05	7.10	3.48	0.17	0.6	1.0	B	15
206	960221	1:09:33.20	42°47.75	2°31.27	7.84	3.03	0.11	0.7	0.9	B	9
207	960221	1:15:10.61	42°47.53	2°32.88	8.40	3.19	0.16	0.6	1.0	B	15
208	960221	1:24:18.80	42°47.08	2°32.95	8.32	2.60	0.08	0.6	0.9	B	7
209	960221	1:26:58.19	42°46.84	2°31.49	7.53	2.45	0.09	0.8	1.5	B	6
210	960221	1:38:44.01	42°47.21	2°32.57	8.12	2.88	0.11	0.6	0.7	B	13
211	960221	1:41:58.75	42°48.03	2°31.84	8.77	3.01	0.13	1.2	1.1	B	9
212	960221	1:44:30.93	42°47.31	2°32.32	8.38	3.14	0.18	0.7	0.9	B	17
213	960221	1:45:44.75	42°46.91	2°32.00	8.48	3.61	0.32	0.9	1.1	B	28
214	960221	1:48:50.23	42°46.95	2°31.67	8.96	2.70	0.10	0.5	0.6	B	13
215	960221	2:06:20.12	42°47.40	2°32.47	7.88	3.37	0.31	0.8	1.4	B	25
216	960221	2:08:02.76	42°46.98	2°33.52	7.84	2.89	0.05	0.5	0.5	B	9
217	960221	2:21:39.15	42°47.17	2°33.37	7.87	2.57	0.07	0.7	0.7	B	9
218	960221	2:29:41.23	42°46.89	2°31.45	7.82	2.58	0.06	0.4	0.6	B	8
219	960221	2:41:22.27	42°47.27	2°31.92	7.98	2.79	0.10	0.8	1.2	B	8
220	960221	2:42:51.84	42°46.99	2°32.84	8.53	2.61	0.11	1.6	1.6	C	7
221	960221	2:47:42.01	42°47.64	2°31.66	8.38	3.14	0.11	0.4	0.7	A	13
222	960221	2:54:20.51	42°47.78	2°32.80	8.66	2.96	0.10	0.4	0.6	B	13
223	960221	3:09:52.36	42°47.11	2°33.78	5.74	2.74	0.07	1.0	1.7	C	7
224	960221	3:12:01.77	42°47.08	2°30.29	7.90	2.75	0.22	1.4	1.8	C	10
225	960221	3:27:27.01	42°47.24	2°32.30	8.71	2.76	0.07	0.7	0.6	B	9
226	960221	3:31:42.10	42°47.19	2°32.61	8.42	3.02	0.19	0.6	0.9	B	21
227	960221	3:32:15.25	42°47.13	2°31.51	8.73	2.45	0.10	1.0	1.0	B	8
228	960221	3:33:19.75	42°47.33	2°32.66	8.92	2.99	0.05	0.5	0.5	B	9
229	960221	3:34:36.74	42°47.68	2°31.18	8.43	3.00	0.11	0.6	0.6	B	13
230	960221	3:38:33.86	42°47.52	2°31.86	7.94	3.32	0.16	0.7	0.8	B	15

No.	Date yymmdd	Time hh:mm:ss	Latitude °N	Longitude °E	Depth km	Ml	rms s	ERH km	ERZ km	Q	n.ph.
231	960221	3:50:47.95	42°47.14	2°32.18	6.97	3.01	0.17	0.9	1.2	B	11
232	960221	3:57:10.43	42°47.51	2°33.98	7.79	2.80	0.04	0.4	0.4	B	9
233	960221	4:07:33.85	42°47.61	2°31.88	7.91	3.16	0.16	0.7	0.8	B	15
234	960221	4:12:11.49	42°47.58	2°32.40	8.34	3.05	0.13	1.0	0.8	C	12
235	960221	4:17:32.27	42°47.30	2°32.14	8.90	2.92	0.12	1.8	0.9	C	9
236	960221	4:30:46.64	42°47.35	2°31.19	8.77	3.02	0.13	0.8	0.9	B	10
237	960221	4:35:04.95	42°47.58	2°32.48	8.30	3.36	0.17	0.6	0.8	B	17
238	960221	5:07:32.74	42°47.08	2°32.56	7.82	2.72	0.06	0.5	1.0	B	6
239	960221	5:11:48.17	42°47.76	2°32.29	8.51	3.44	0.18	0.6	0.9	B	17
240	960221	5:17:28.01	42°47.30	2°31.75	8.20	2.95	0.12	0.6	1.0	B	9
241	960221	5:33:58.96	42°47.54	2°31.87	8.48	3.31	0.15	0.8	0.9	B	12
242	960221	5:50:05.09	42°47.47	2°33.25	7.60	3.34	0.19	0.9	1.0	C	13
243	960221	5:54:09.10	42°47.54	2°32.57	8.97	2.80	0.08	1.8	1.4	C	6
244	960221	6:06:35.89	42°47.31	2°32.69	8.60	3.04	0.06	0.6	0.5	B	9
245	960221	6:07:08.84	42°48.13	2°27.80	5.51	3.00	0.29	1.8	2.4	C	9
246	960221	6:20:35.72	42°47.46	2°32.44	7.11	3.08	0.25	1.0	1.5	B	14
247	960221	6:27:30.47	42°47.27	2°32.38	7.95	3.11	0.16	0.7	1.2	B	11
248	960221	6:43:36.23	42°47.24	2°32.43	7.34	3.22	0.18	0.7	1.2	B	13
249	960221	6:50:12.64	42°46.74	2°31.50	10.05	3.62	0.33	0.9	1.1	B	28
250	960221	7:11:04.07	42°47.45	2°31.11	8.76	3.20	0.12	0.7	0.8	B	12
251	960221	7:17:07.30	42°47.84	2°31.79	7.43	3.23	0.14	0.6	0.8	B	13
252	960221	7:54:24.00	42°47.06	2°33.56	7.37	3.03	0.07	1.0	1.2	B	7
253	960221	7:60:04.56	42°47.10	2°32.48	8.33	2.66	0.07	1.0	1.0	B	7
254	960221	8:07:05.54	42°47.26	2°31.21	8.83	2.57	0.14	1.2	0.9	B	11
255	960221	8:21:05.87	42°47.46	2°32.70	8.42	2.62	0.12	0.6	0.9	B	12
256	960221	8:48:39.10	42°47.51	2°32.64	7.98	2.48	0.17	2.4	2.2	C	7
257	960221	8:49:56.67	42°48.02	2°30.40	9.40	2.46	0.07	1.5	0.9	C	6
258	960221	9:26:31.15	42°47.70	2°32.02	9.42	3.03	0.15	0.9	0.9	C	13
259	960221	9:32:32.27	42°47.73	2°33.26	8.19	2.60	0.14	1.9	1.8	C	7
260	960221	10:05:58.20	42°47.59	2°31.93	8.46	2.87	0.15	0.9	1.0	B	12
261	960221	10:37:16.15	42°47.31	2°33.59	7.17	3.31	0.13	0.9	1.0	B	11
262	960221	11:21:33.95	42°47.83	2°31.59	8.95	3.31	0.15	0.8	1.0	B	12
263	960221	11:30:34.21	42°47.75	2°33.68	8.96	2.94	0.13	1.3	0.9	C	11
264	960221	11:52:03.44	42°47.53	2°32.91	9.09	3.12	0.13	1.2	0.9	C	10
265	960221	11:54:03.79	42°47.68	2°30.91	7.55	3.32	0.26	0.8	1.2	B	19
266	960221	12:07:22.33	42°48.10	2°30.48	9.90	2.65	0.04	1.2	0.6	C	6
267	960221	12:44:44.14	42°47.14	2°32.22	8.34	2.76	0.07	0.7	0.7	B	9
268	960221	12:58:26.50	42°47.18	2°32.51	8.49	2.96	0.08	0.5	0.7	B	10
269	960221	12:60:31.42	42°47.30	2°32.67	9.24	2.58	0.04	0.3	0.4	B	8
270	960221	13:18:15.86	42°47.12	2°32.60	8.44	3.02	0.07	0.4	0.6	B	10
271	960221	13:23:45.30	42°47.12	2°33.00	6.69	2.82	0.05	0.7	0.9	B	7
272	960221	14:07:09.99	42°47.23	2°33.24	7.65	3.02	0.05	0.6	0.6	B	8
273	960221	14:07:53.43	42°46.79	2°31.85	9.49	3.10	0.09	0.9	0.8	B	9
274	960221	14:40:02.93	42°47.51	2°32.76	8.70	3.19	0.15	0.8	0.8	B	14
275	960221	15:38:00.89	42°47.29	2°31.88	8.86	3.43	0.30	1.0	1.3	B	19
276	960221	16:23:32.24	42°46.76	2°32.75	7.68	2.80	0.04	0.9	0.7	B	6
277	960221	16:51:54.75	42°46.98	2°32.75	8.00	3.21	0.05	0.5	0.4	B	9
278	960221	17:02:17.76	42°46.76	2°33.94	9.21	3.04	0.13	1.3	1.2	C	9
279	960221	19:08:53.92	42°48.03	2°32.58	7.04	2.73	0.22	1.3	1.4	C	12
280	960221	19:26:42.00	42°46.73	2°33.15	6.71	2.40	0.09	0.8	1.2	B	7
281	960221	19:34:45.62	42°46.86	2°31.30	8.33	3.67	0.15	0.5	0.8	A	17
282	960221	19:41:10.74	42°46.98	2°31.64	9.16	3.00	0.07	0.6	0.6	B	10
283	960221	19:60:15.13	42°48.10	2°33.34	8.55	2.46	0.09	0.7	0.7	B	11
284	960221	20:51:46.23	42°48.01	2°32.33	8.56	2.55	0.19	0.9	1.1	C	13
285	960221	20:53:50.04	42°46.95	2°33.24	7.34	2.44	0.06	0.8	1.0	B	7
286	960221	21:01:03.07	42°47.11	2°32.85	9.18	2.54	0.08	0.9	1.0	B	7
287	960221	22:54:00.84	42°47.08	2°32.85	7.11	2.77	0.19	0.9	1.4	B	11
288	960221	23:15:27.40	42°47.08	2°29.89	8.64	2.66	0.16	2.3	1.4	C	9
289	960221	23:18:26.45	42°48.38	2°32.15	7.66	2.87	0.16	0.8	1.0	B	12
290	960222	0:21:31.26	42°48.04	2°32.19	8.68	3.26	0.21	1.0	1.3	B	13
291	960222	0:28:34.91	42°47.88	2°30.81	9.24	2.78	0.19	2.1	1.5	C	10
292	960222	1:06:40.13	42°46.64	2°32.94	8.82	2.90	0.10	2.0	1.3	C	7
293	960222	2:19:10.02	42°47.47	2°32.61	8.64	3.30	0.18	1.2	1.1	C	12

No.	Date yymmdd	Time hh:mm:ss	Latitude °N	Longitude °E	Depth km	M1	rms s	ERH km	ERZ km	Q	n.ph.
294	960222	2:32:00.50	42°47.69	2°32.33	8.84	3.07	0.17	1.0	1.0	C	13
295	960222	2:52:25.55	42°46.96	2°33.08	8.21	2.55	0.04	0.5	0.6	B	7
296	960222	2:53:37.06	42°47.20	2°32.37	8.91	3.55	0.21	0.6	0.8	B	25
297	960222	3:12:34.40	42°48.03	2°32.24	9.09	2.83	0.18	1.0	1.1	C	13
298	960222	3:14:32.37	42°47.51	2°32.21	9.05	2.97	0.18	2.2	1.5	C	9
299	960222	4:14:58.50	42°47.57	2°32.60	8.76	2.72	0.08	0.5	0.6	B	11
300	960222	4:17:39.38	42°47.21	2°32.86	9.48	3.06	0.20	1.2	1.2	C	13
301	960222	4:41:13.53	42°47.21	2°33.10	10.00	2.90	0.19	2.1	1.6	C	10
302	960222	4:43:19.06	42°47.08	2°32.78	8.05	2.50	0.10	0.6	0.8	B	11
303	960222	5:39:39.96	42°47.32	2°29.89	8.96	2.61	0.19	2.8	1.6	C	9
304	960222	6:36:26.37	42°47.41	2°33.55	8.89	3.04	0.09	0.6	0.7	B	11
305	960222	7:07:32.03	42°47.20	2°32.13	8.15	3.17	0.17	0.5	0.8	B	20
306	960222	8:10:55.07	42°47.55	2°32.91	9.89	3.08	0.20	1.1	0.9	C	16
307	960222	8:15:42.63	42°47.48	2°32.87	9.93	3.16	0.20	1.0	1.0	C	17
308	960222	10:59:51.43	42°46.72	2°34.42	7.22	3.33	0.10	0.7	0.9	B	11
309	960222	14:30:31.45	42°47.41	2°31.33	10.31	2.82	0.11	1.6	1.0	B	8
310	960222	15:50:24.99	42°47.24	2°33.23	8.02	2.59	0.05	0.7	0.7	B	7
311	960222	17:27:48.11	42°47.90	2°32.00	10.00	3.07	0.25	1.8	2.0	B	10
312	960222	17:29:41.80	42°46.96	2°31.47	8.42	2.77	0.06	0.4	0.7	B	8
313	960222	19:56:32.56	42°46.96	2°33.64	7.98	2.67	0.06	1.0	1.2	B	6
314	960222	20:09:57.06	42°47.89	2°34.21	8.55	2.66	0.18	1.3	1.8	B	9
315	960222	22:34:39.87	42°47.07	2°32.97	7.99	2.78	0.06	0.4	0.6	B	9
316	960222	23:21:57.55	42°47.61	2°32.35	8.96	2.92	0.06	0.5	0.7	B	7
317	960223	0:06:32.90	42°47.44	2°31.19	9.18	3.63	0.11	0.3	0.4	A	20
318	960223	0:32:21.11	42°47.89	2°32.89	8.66	2.75	0.20	1.5	2.0	B	9
319	960223	0:32:34.86	42°47.04	2°32.01	10.00	3.37	0.24	1.4	1.7	B	11
320	960223	0:41:50.43	42°47.42	2°31.68	8.07	3.26	0.12	0.7	1.2	B	10
321	960223	1:03:03.39	42°47.08	2°32.84	8.31	3.02	0.05	0.8	0.9	B	6
322	960223	1:05:01.18	42°47.04	2°33.38	7.44	2.50	0.05	0.7	0.9	B	7
323	960223	1:06:11.84	42°47.11	2°33.31	7.97	2.96	0.03	0.4	0.4	B	7
324	960223	2:06:37.53	42°47.27	2°33.30	10.00	2.86	0.28	2.6	2.7	C	8
325	960223	3:28:51.75	42°47.39	2°31.94	10.06	3.25	0.26	1.1	1.4	B	14
326	960223	4:05:34.74	42°46.97	2°31.50	8.08	2.77	0.08	0.7	1.3	B	6
327	960223	4:12:08.08	42°46.99	2°32.44	6.72	2.95	0.12	0.7	1.5	B	8
328	960223	4:15:03.73	42°47.20	2°32.79	7.76	3.00	0.07	0.6	1.0	B	7
329	960223	4:18:18.83	42°46.74	2°32.35	7.99	3.37	0.15	0.5	0.9	B	15
330	960223	4:24:05.96	42°47.19	2°32.40	8.52	2.32	0.06	0.5	0.9	B	6
331	960223	4:29:36.00	42°47.37	2°33.10	8.56	2.89	0.27	2.0	2.5	C	9
332	960223	4:33:42.59	42°47.44	2°31.50	8.08	2.99	0.10	1.1	1.4	B	7
333	960223	6:55:20.56	42°46.71	2°33.00	8.81	2.86	0.26	1.5	2.0	B	11
334	960223	7:20:07.74	42°47.28	2°33.01	10.00	2.70	0.27	2.2	2.4	C	9
335	960223	7:22:27.71	42°46.82	2°32.54	3.68	2.57	0.24	1.2	2.1	C	9
336	960223	7:46:03.43	42°47.17	2°32.58	10.00	2.85	0.28	1.4	1.9	B	12

## APPENDIX B

Focal mechanisms. Lower equal-area hemisphere showing compressional (+) and dilatational (-) arrivals.



## APPENDIX C

Focal mechanisms of the stress tensor inversion. Lower equal-area hemisphere showing compressional (+) and dilatational (-) arrivals.

